Combined experimental, computational studies (synthesis, crystal structural, DFT calculations, spectral analysis) and biological evaluation of the new homonuclear complexDi-μ-benzoato-bis [benzoatodipyridinecobalt (II)]

Oussama Khaoua, Noura Benbellat, Samira Zeroual, Soumia Mouffouk, Stéphane Golhen, Abdelkrim Gouasmia, Henry Chermette, Hamada Haba

Combined experimental, computational studies (synthesis, crystal structural, DFT calculations, spectral analysis) and biological evaluation of the new homonuclear complexDi-μ-benzoato-bis [benzoatodipyridine-cobalt (II)]

Oussama KHAOUA[a], Noura BENBELLAT*[ad], Samira ZEROUAL[a], Soumia MOUFFOUK[b], Stéphane GOLHEN[c], Abdelkrim GOUASMIA[d], Henry CHERMETTE[†e] and Hamada HABA[b].

[a]*Laboratoire de Chimie des Matériaux et des Vivantes : Activité & Réactivité (LCMVAR), Département de chimie, Faculté des sciences de la matière, Université de Batna-1, Algérie.*

[b]*Laboratoire de Chimie et Chimie de l'Environnement, Département de chimie (LCCE), Faculté des sciences de la matière, Université de Batna-1, Algérie.*

[c]*Univ Rennes, CNRS, ISCR (Institut des Sciences Chimiques de Rennes)−UMR 6226, F-35000 Rennes, France.*

[d]*Laboratoire des Matériaux Organiques et Hétérochimie, Faculté des sciences et de la technologie, Université Larbi Tébessi, Tébessa, Algérie.*

[e]*Institut des Sciences Analytiques de Lyon, UMR 5280 CNRS-Université Lyon 1,F-69622 VILLEURBANNE Cedex, France.*

Corresponding authors: Noura Benbellat Tel: +213 671214105; Fax: +213 33319015; E-mail addresses:

* noura.benbellat@univ-batna.dz;benbellat_nora@yahoo.fr

[†]Henry.Chermette@univ-lyon1.fr

Highlights

- The single crystal was obtained

- Biological activities were assessed

- TD/DFT calculations were performed to support experimental results

- Non-Covalent Interaction (NCI) was carried out

- The Fukui parameters were investigated

Graphical Abstract

15 g of benzoic acid + hot ethanol (200 mL) → Filtration into 8.5 g of basic cobalt II carbonate → Heat under reflux for 6h. + 20 mL of pyridine → Filtration

X-ray structure

Biological activities

Computational investigation

Characterization of the molecular structure
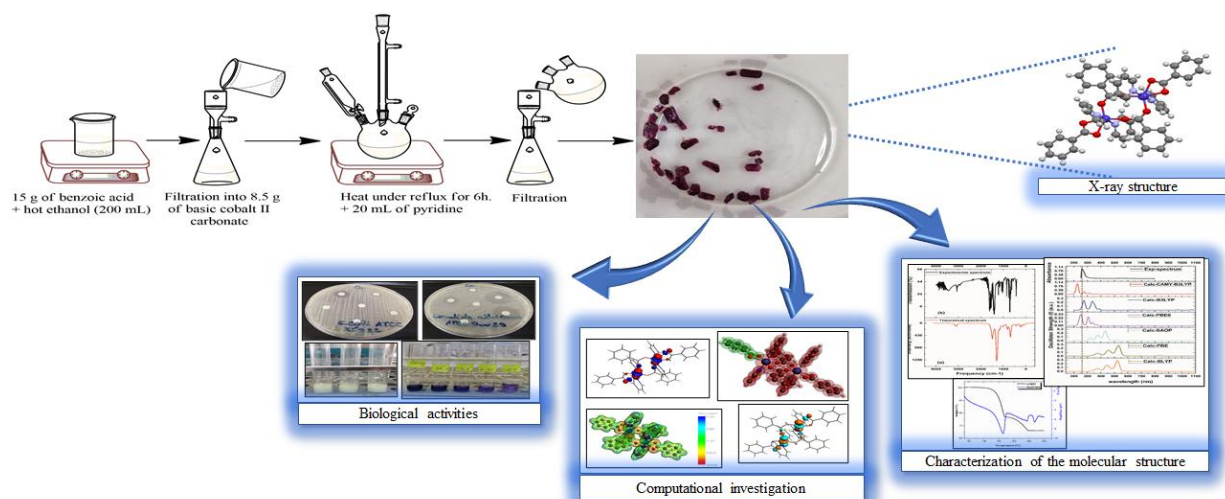
ABSTRACT

A binuclear cobalt(II) benzoate complex with pyridine as auxiliary ligands has been synthesized and identified by UV–Vis, IR spectroscopy, and TG-DTA analysis. The molecular structure of the complex was determined by single-crystal X-ray diffraction (SCXRD). Thermogravimetric analysis shows two steps decomposition of the present complex. The Co (II) ions are in a distorted octahedral environment $[CoN_2O_4]$. The crystal structure was stabilized by different intramolecular/ intermolecular interactions, including Van der Waals, hydrogen bonding, donor-acceptor, and π-π interactions between the pyridine rings. Furthermore, all density functional theory (DFT) calculations have been performed in the gas phase using the GGA-BLYP functional and the TZP basis set, and for the Time-Dependent Density Functional Theory (TD-DFT) calculations, several functionals have been used, namely the GGA BLYP and PBE, the hybrids B3LYP and PBE0, the SAOP potential model, and finally the range-separated CAMY-B3LYP functional with the TZP basis set. Good consistency was observed between the calculated and the experimental results. The bond dissociation energies (BDE) were calculated using the fragment analysis. The intermolecular interactions were investigated through the Molecular Electrostatic Potential (MEP) and supported by Hirshfeld charges analysis. To characterize the non-covalent interactions in the complex, (NCI plot) index has been computed and supported by AIM analysis. Also, the global and local reactivity descriptors have been calculated to highlight the reactive sites in the molecular structure. Moreover, the antimicrobial activity was evaluated by agar disk diffusion assay against seven pathogenic strains, and the antioxidant activity was estimated using four different techniques. In addition, the *in vitro* anti-inflammatory activity was assessed by the albumin denaturation method.

1. Introduction

Coordination chemistry of transition metals based on Co has gained importance for its capability to bind dioxygen reversibly [1]. Especially, those possessing an auxiliary ligand have been a subject of intensive research in recent years [2-4]. On the purpose of their interest structures, some of these hybrid compounds exhibit interesting applications which have been expanded to pharmacological and biological activities such as antimicrobial [5], anti-inflammatory [6]anticancer [7], antidiabetic, antimalaria [8], and antioxidant activities in addition to their catalytic properties in redox reactions [9], benzoate is used as an antimicrobial agent in edible coatings [10]. Also, sodium benzoate is used in cosmetic and food industries. The nitrogen atoms of heterocyclic ligands like isoquinoline and pyridine are easily coordinated to the metal center [11]. The impressive effectiveness of antimicrobial agents has stimulated their extended and frequent applications in human and animal health. This created selective pressure on microbial groups, which led to the emergence of resistant microbes. Therefore, it is necessary to find novel strategies for the improvement of new drugs that target multiple cellular processes to enhance their efficacy against multiple micro-organisms, including bacteria, viruses, and fungi. Recently, antibiotic development studies have shown that metal ion complexes caused various types of damage to microbial cells due to membrane degradation, protein disruption, and oxidative stress. These particular modes of action, together with the wide range of 3D geometries that metal complexes can adopt, make them suitable for the development of new antimicrobial drugs [12].

Reactive oxygen species (ROS) are chemical species comprising free radicals such as superoxide anion ($O_2^{\bullet-}$), hydroxyl radical ($\bullet OH$), peroxyl radical ($ROO\bullet$) and alkoxyl radical ($RO\bullet$), as well as non-radical molecules like hydrogen peroxide (H_2O_2) and singlet oxygen ($^1O_2$). These species are beneficial to live organisms at low concentrations [13] However, the uncontrolled production of these species accompanied by a dysfunction of the antioxidant systems causes several metabolic alterations and damages the biological macromolecules (lipids, DNA, and proteins). Thus, this could lead to many diseases such as cancer, diabetes, asthma, aging, cardiovascular, neurodegenerative, and inflammatory

diseases [14]. Therefore, research on metal complexes with antioxidant properties is a promising strategy for the development of new effective antioxidants useful in medicine, pharmaceutical, and food industries, as well as other fields [15].

The aim of the present paper is the synthesis, characterization, spectroscopic analysis, DFT calculations, and biological activities of the new cobalt (II) coordination complex based on pyridine and benzoate ligands. To the best of our knowledge, there are no previous reports on experimental and theoretical calculations, as well as biological properties of the studied compound di-μ-benzoato-bis [benzoatodipyridine-cobalt (II)], also named by the (μ-benzoato)-(μ-benzoato)-bis(benzoato)-[tetrakis(pyridine)]-di-cobalt.

2. Materials and methods

2.1. Materials

In order to obtain crystals of high quality and to achieve good handling conditions, purification of starting materials was found to be an important step and hence, the recrystallized salts were used for the growth of crystals of the studied material. All solvents used in the experiments were purchased from PROLAB, MERK EUROLAB. 2,2-diphenyl-1-picrylhydrazyl (DPPH), trichloroacetic acid (TCA), potassium ferricyanide ($K_3Fe[CN]_6$), ferric chloride ($FeCl_3$), dimethyl sulfoxide (DMSO), hydrogen peroxide (H_2O_2), and ammonium molybdate ($(NH_4)_2MoO_4$) were obtained from Sigma-Aldrich Chemie and FlukaChemie. The reference molecules used in this study as butylate hydroxytoluene (BHT) ($C_{15}H_{24}O$), butylate hydroxyanisole (BHA) ($C_{11}H_{16}O_2$) and ascorbic acid ($C_6H_8O_6$) were purchased from Sigma-Aldrich Co, ST Lowis, Mo.

2.2. Characterization techniques

The FT-IR spectrum was registered in the 400–4000 cm^{-1}region with a Perkin-Elmer spectrometer using ATR techniques. The electronic spectrum was recorded in DMSO as solvent with a

5

spectrophotometer UV-Vis Thermo Scientific Evolution 220 model in the 240–800 nm region. UV-Vis spectrophotometer SHIMADZU UV-1700 was used for the biological measurements. Thermal analysis was realized on a Mettler Toledo TGA/DSC lab sys Evo-gas system using a UMX1 balance and platinum crucible. TG/DTA measurement was taken on a 21.2 mg sample in argon atmosphere, within the 40–350 °C temperature range at Batna-1 University. Crystallographic data of purple crystal were collected at 150K on an APEXII Bruker-AXS diffractometer equipped with graphite monochromated Mo–Kα radiation. The structure was solved by direct methods with SIR-97 [16], which revealed the non-hydrogen atoms of the molecules. Refinement was performed by full-matrix least-square techniques based on F^2 with SHELXL [17] with the aid of the WINGX [18] program. All non-hydrogen atoms were refined with anisotropic thermal.

2.3. Micro-organisms

The bacterial strains from the American Type Culture Collection (*Escherichia coli* ATCC 25922, *Staphylococcus aureus* ATCC 25923, *Pseudomonas aeruginosa* ATCC 1117) and the fungi strain (*Candida albicans* ATCC 90029), as well as the pathogenic bacteria (*Escherichia coli, Klebsillapneumonae* and *Staphylococcus aureus*), were supplied by the Laboratory of Bacteriology, University Hospital Center-Batna (CHU).

2.4. Biological activities

2.4.1. Antimicrobial activity

The antibacterial activity of the complex "di-μ-benzoato-bis [benzoatodipyridine-cobalt (II)" with general formula $Co_2(\mu_2(\eta_1-\eta_1)-Benz)_2(\mu_1-Benz)_2(Pyr)_4$ was evaluated by the agar disk diffusion assay [19], against six bacterial strains. One or several colonies from each pure culture were transferred into 5 mL of nutrient broth. The bacterial suspension was homogenized and incubated at 37 °C for 10-24 hours. After incubation, a reading of the optical density (OD) of 1 mL of inoculum was made by a spectrophotometer at 625 nm. Opacity must be equivalent to 0.5 McFarland. A sample from each inoculum was used to inoculate Petri dishes containing Mueller Hinton by swabbing technique. Wathman

paper discs (6 mm) were impregnated with 10 µL of the tested complex solutions at different concentrations (62.5, 125, 250, 500, and 1000 µg/mL) and filed carefully on the surface of the inoculated agar with sterile forceps. The discs of the negative controls were impregnated with dimethyl sulfoxide (DMSO). The Petri dishes were incubated at 37 °C for 24h. The assays were performed in triplicate (three boxes for each concentration of the solution and each strain). The results were given by the diameters of zones of inhibition around the discs produced and the values were expressed as means ± SD of three measurements ($p < 0.05$). The same experimental procedure for antibacterial activity was applied to estimate antifungal activity using Sabouraud agar. The Petri dishes were incubated at 30 °C for 72 hours.

2.4.2. Antioxidant activities

The antioxidant activity of the $Co_2(\mu_2(\eta_1-\eta_1)-Benz)_2(\mu_1-Benz)_2(Pyr)_4$ complex was evaluated *in vitro* via their ability to scavenge free radicals and to reduce transition metals using four different techniques.

2.4.2.1. Ferric reducing antioxidant power (FRAP)

To evaluate the ferric reducing capacity metal complex, 100 µL of sample solutions were added to 500 µL of phosphate buffer (0.2 M; pH 6.6) and 500 µL of ferrocyamide solution (1%). The mixture was incubated for 20 min at 50 °C and then, 500 µL of TCA (10 %) were added. After incubation, the mixture was centrifuged for 10 min at 3000 rpm. 500 µL of the supernatant solution were mixed with 500 µL of distilled water and 100 µL of $FeCl_3$ (0.1 %), the values of the absorbance were recorded at 700 nm. The reducing antioxidant activity was measured using the calibration curve of the ascorbic acid and the results were expressed as µg EAA/mg [20].

2.4.2.2. Total antioxidant capacity (TAC)

The total antioxidant capacity of the tested complex was determined by phosphomolybdenum assay [20]. 100 µL of the sample were added to 900 µL of reagents mixture (0.6 M sulfuric acid, 28 mM sodium phosphate, and 4 mM ammonium molybdate). The prepared solutions were incubated at 95 °C for 90 min. After cooling at room temperature, the absorbance was read at 695 nm. The total antioxidant

7

capacity was calculated according to the calibration curve prepared from ascorbic acid and the results were expressed as µg EAA/mg.

2.4.2.3. Hydrogen peroxide scavenging capacity

The hydrogen peroxide scavenging assay was performed according to the method of Ruch et al. [21]. A solution of hydrogen peroxide (H_2O_2, 43 mM) was prepared in phosphate buffer (0.1 M, pH 7.4). All the samples (Co (II)-complex and antioxidant standards) were prepared at the concentration of 100 µg/mL in phosphate buffer. The prepared samples were added to 0.6 mL of H_2O_2 solution. The absorbance of the reaction mixture was read at 230 nm after 10 minutes of incubation. The blank solution containing the phosphate buffer without hydrogen peroxide was used to calculate the percentages of inhibition as follows:

$$Activity \ (\%) = \left[\left(A_{Blank} - A_{Sample} \right) / A_{Blank} \right] \times 100$$

A_{Blank} is the absorbance of blank and A_{Sample} is the absorbance of the sample. The experiments were performed in triplicate and the results were transmitted as mean (values ± SD).

2.4.2.4. DPPH radical scavenging activity

The scavenging of the free radical DPPH was estimated by the method described by Blois [22]. 25 µL of sample solutions (complex or standards) at different concentrations were added to 975 µL of DPPH (0.025 mg/mL), then the mixture was kept in the darkness at room temperature for 30 minutes. The blank was prepared by adding 25 µL of methanol to 975 µL of DPPH reagent and the absorbance was measured at 517 nm. The percentage of DPPH radical-scavenging activity of each sample was calculated as follows:

$$Activity \ (\%) = \left[\left(A_{Blank} - A_{Sample} \right) / A_{Blank} \right] \times 100$$

A_{Blank} is the absorbance of blank and A_{Sample} is the absorbance of the sample. The experiments were performed in triplicate and the results were transmitted as mean (values ± SD).

2.4.3. Egg albumin denaturation method

The anti-inflammatory activity was tested by egg albumin denaturation method described by Sunmathiet al. [23]. 2 mL of different concentrations of the sample or diclofenac sodium as a standard drug were added to a reaction mixture containing 200 µL of egg albumin (from fresh hen's egg) and 2.8 mL of phosphate-buffered saline (PBS, pH 6.4). The obtained solutions were incubated at 37 °C for 15 min and then heated at 70 °C for 5 min. After cooling at room temperature, the absorbance was measured at 660 nm. A control solution was prepared by replacing the sample with double-distilled water and the percentage of inhibition of protein denaturation was calculated as follows:

$$\% \ inhibition = 100 \times \left[V_S / V_C - 1 \right]$$

Where, V_S: absorbance of the sample, Vc: absorbance of control. Each experiment was done in triplicate and the results were recorded as a mean (values $\pm$ SD).

2.4.4. Statistical analysis

The results were given as the means $\pm$ S.D ($p < 0.05$) for three replicates for each sample and values were calculated by linear regression analysis and expressed as: µg EAA/mg for total antioxidant capacity and ferric reducing antioxidant power, IC_{50} for DPPH free radical-scavenging assay and as a percentage of inhibition (%) for the anti-inflammatory and hydrogen peroxide scavenging assays. Significant differences between means were determined by one-way ANOVA, followed by the Duncan test and all the statistics were carried out using Graph Pad prism 5.04

3. Computational details

Full geometry optimization was carried out in the gas phase on the dimeric cobalt complex at their neutral, 1+, 2+ and 3+ oxidation states, by the density functional theory (DFT) method using the ADF quantum chemistry package. [24] The starting geometry for the calculation was taken from the experimentally single-crystal structure. All the calculations were treated at the Generalized Gradient Approximation (GGA) level, with the BLYP exchange-correlation functional [25] (Becke for exchange

[25]; Lee, Yang, Parr for correlation [26]), with the TZP basis set. The vibrational frequency computations were performed to ensure that the achieved optimized geometry represents local minima. The Time-Dependent DFT (TD-DFT) method [27] has been applied to calculate the excited states of the dimeric motif in gas phase. Their corresponding electronic transitions at the singlet and triplet spin states are investigated. An AIM analysis was performed with DGrid/Basin program [28], the critical points were represented by the Chem craft 1.4 program [29]. The Bond Decomposition Energy (BDE) developed by Ziegler [30] gives information on the type of links. It can be expressed by three terms; orbital energy, electrostatic interaction, and Pauli component. The calculation of the "Non-Covalent Interaction" plot (NCI plot) and the molecular electrostatic potential properties have been investigated. Fukui indices were calculated using the analytical method considering Hirshfeld atomic charges. The gap energy, ionization potential (I), electron affinity (A), chemical potential (μ) and hardness (η) can be calculated by the Koopmans' theorem [31], softness (S), electronegativity (χ) and global electrophilicity index (ω) were all examined using the equations (3-8) [32–34].

4. Results and discussion

4.1. Preparation of the complex

The synthesis of the title complex was carried as follows: 15 g, (1 eq) of benzoic acid were dissolved in hot ethanol (200 mL). The resulting solution was stirred for 2h, filtered into (8.5 g) of basic cobalt II carbonate ($2Co (CO_3) . 3Co(OH)_2$) and heated under reflux for 6h. Then, 20 mL, (2 eq) of pyridine was added to the resulting ethanolic solution and heated for 1 hour again, and immediately filtered to remove unreacted species. The violet single crystals precipitated on coaling, washed with cold ethanol and dried, yielded 2.5 g (5.3 %).

4.2. Description of the molecular structure

The centrosymmetric dinuclear $Co_2(\mu_2(\eta_1-\eta_1)-Benz)_2(\mu_1-Benz)_2(Pyr)_4$ compound crystallizes in the centrosymmetric $P2_1/c$ space group (Details are given in Table 1). The distorted octahedral coordination

sphere of Co^{II} is made up of 4 oxygen atoms from 3 benzoate ions, one acting as $\mu_1(\eta_1$-$\eta_1)$ thanks to O1 and O2 atoms, two centrosymmetric bridging $\mu_2(\eta_1$-$\eta_1)$ benzoate ions thanks to O3 and O4^i (i: -x, 1-y, 1-z) and two nitrogen atoms (N1 and N2) in trans positions from two pyridine molecules) (see Figure 1).

Table 1. Crystal data and structure refinement for $Co_2(\mu_2(\eta_1-\eta_1)-Benz)_2(\mu_1-Benz)_2(Pyr)_4$

Empirical formula	C48 H40 Co2 N4 O8
Formula weight	918.70
Temperature	150(2) K
Wavelength	0.71073 Å
Crystal system	Monoclinic
Space group	P 2_1/c
Unit cell dimensions	a = 12.5200(6)Å, b = 8.2570(3)Å, c = 20.5277(10)Å
	β= 100.456(2)°.
Volume	2086.87(16) Å^3
Z	2
Density (calculated)	1.462 Mg/m^3
Absorption coefficient	0.856 mm^{-1}
F(000)	948
Theta range for data collection	2.366 to 27.502°.
Index ranges	-16≤h≤15, -10≤k≤10, 0≤l≤26
Reflections collected	7947
Independent reflections	4761 [R(int) = 0.0269]
Completeness to theta = 25.242°	99.9 %
Refinement method	Full-matrix least-squares on F^2

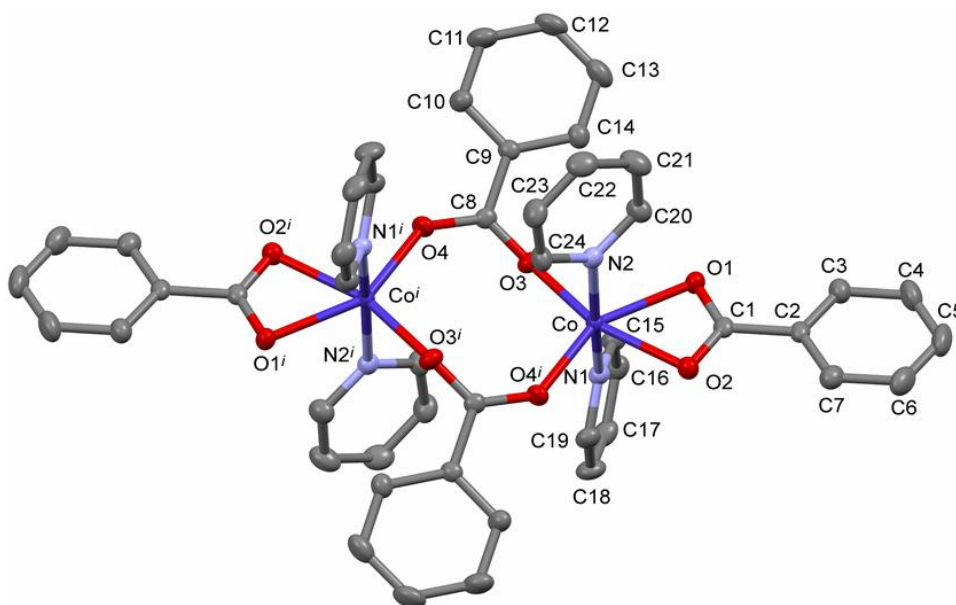| Data / restraints / parameters	4761 / 0 / 280
Goodness-of-fit on F^2	0.925
Final R indices [I>2sigma(I)]	R1 = 0.0336, wR2 = 0.0866
R indices (all data)	R1 = 0.0468, wR2 = 0.0933
Largest diff. peak and hole	0.339 and -0.455 e.Å^{-3}

Figure 1: Labelling scheme of $Co_2(\mu_2(\eta_1-\eta_1)-Benz)_2(\mu_1-Benz)_2(Pyr)_4$ with symmetry i : -x, 1-y, 1-z

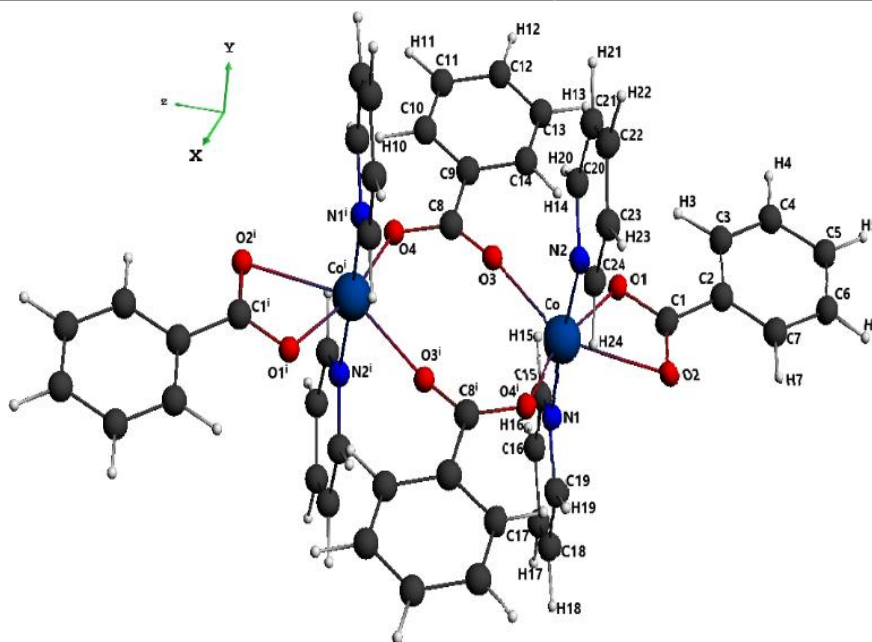**Figure 2**. Optimized molecular structure of $Co_2(\mu_2(\eta_1-\eta_1)-Benz)_2(\mu_1-Benz)_2(Pyr)_4$.

The octahedral coordination sphere of cobalt ions is distorted, with bonds lengths ranging from 2.0170(13) to 2.2089(13)° and angles from 86.12(5)° to 106.55(5)°. The geometries of CO_2 fragments of μ_2 bridging and of μ_1 benzoates are quite similar with O-C-O angles of 125.18(17)° and 120.56(17)° respectively (see Table 2). The phenyl ring of the μ_1 benzoate form an angle of 5.61(22)° with the CO_2 plane, the Co^{II} being in the phenyl plan (0.0044(43) Å above) whereas those of the μ_2 benzoate form an angle of 10.55(7)°, the cobalt ion is 0.416(4) Å below the phenyl ring.

The present molecular structure was fully optimized at their neutral and oxidized states 1+, 2+, and 3+ using the DFT-BLYP method at TZP level of theory (see Figure 2). The results were compared to the X-ray crystallographic parameters (Table 2). All the chelating calculated geometrical parameters, bonds length, angles, and dihedral angles concern one cobalt (II) ion and its environment.

Table 2: Selected calculated and experimental geometrical parameters bond lengths [Å] and angles [°] for

the complex.

	Experimental values	Calculated values			
Oxidation state	**(0)**	**(0)**	**(1+)**	**(2+)**	**(3+)**
Bond length					
Co-O(3)	2.0170(13)	1.964	1.982	1.963	1.965
Co-O(2)	2.1514(13)	1.989	2.046	1.979	2.042
Co-N(2)	2. 1659(15)	1.975	1.992	2.009	2.018
O(1)-C(1)	1.267(2)	1.262	1.290	1.305	1.296
O(3)-C(8)	1.254(2)	1.302	1.289	1.282	1.292
Co-O(4)^i	2. 0310(12)	2.364	2.081	1.972	1.969
Co-N(1)	2. 1511(15)	1.980	2.003	2.019	2.027
Co-O(1)	2. 2089(13)	2.499	2.099	1.971	2.047
O(2)-C(1)	1.268(2)	1.308	1.296	1.303	1.300
O(4)-C(8)	1.257(2)	1.254	1.268	1.278	1.284
Bond angles					
O(3)-Co-O(4)^i	106.55(5)	108.60	106.80	110.10	102.0
O(3)-Co-N(2)	87.34(5)	90.70	92.40	92.20	92.40
O(3)-Co-O(2)	162.01(5)	165.30	160.60	158.40	158.80
O(2)-Co-N(2)	92.09(5)	89.60	89.30	89.00	88.10
O(4)^i-Co-O(2)	91.35(5)	86.20	92.20	91.40	99.10
O(4)^i-Co-N(2)	97.76(5)	92.50	94.60	92.70	95.00

N(1)-Co-O(1)	85.07(5)	88.90	88.40	88.70	87.10
N(1)-Co-N(2)	170.92(6)	177.50	176.50	177.30	175.0
O(3)-Co-N(1)	86.12(5)	89.80	88.30	89.20	89.00
O(3)-Co-O(1)	101.38(5)	106.60	96.60	91.60	94.40
O(2)-Co-N(1)	92.18(5)	89.40	89.00	88.90	89.10
O(2)-Co-O(1)	60.63(5)	58.70	64.20	66.80	64.50
O(4)^i-Co-N(1)	90.14(5)	89.60	88.50	89.00	89.00
O(4)^i-Co-O(1)	151.27(5)	144.80	156.30	158.10	163.10
N(2)-Co-O(1)	90.06(5)	88.70	88.20	88.70	88.50
O(3)-C(8)-O(4)	125.18(17)	126.60	127.40	128.60	123.30
O(1)-C(1)-O(2)	120.56(17)	121.50	116.90	113.10	114.40
Energy (eV)		-643.2	-639.2	-631.8	-619.6

Symmetry transformations used to generate equivalent atoms *i*: -x,-y+1,-z+1

According to the structure represented in (Figure 3-a), all intermolecular contact shorter than the van der Waals radii are developed in the *bc* plane: between hydrogen and oxygen atom O2 from $\mu_1$benzoate O2…H18^{ii} = 2.477 Å, O2…H16^{iii} = 2.597 Å and between phenyl ring of from $\mu_2$benzoate C9…H22^{iv} = 2.764 Å. (*ii*: x, ½+y, 3/2-z; *iii* : x, y+1, z; *iv* : x, y-1, z). The intramolecular interactions (Figure 3-b) do exhibit two forms: the first type is observed between the H-pyridine and O-(μ_1−Benz) ring H24-----O3 and H19-----O4, the same type of interaction is also observed between H-pyridine rings and oxygen atom of the ($\mu_2(\eta_1-\eta_1)$−Benz); H20---O1 and H15---O1. The second type is the chelation contacts, it is observed between cis pyridine rings, they are mentioned as H23---C17.
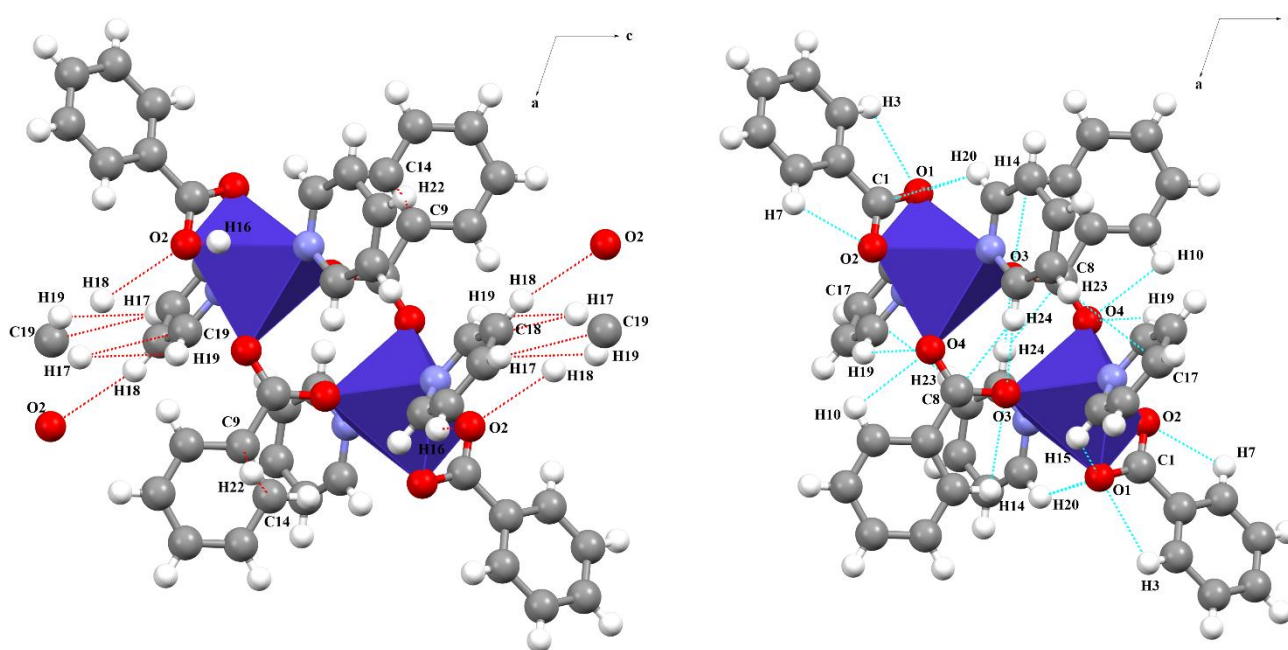
Figure 3: View down crystallographic 'b' axis (a): Intermolecular interactions contacts (b): Intramolecular interactions contacts

In addition to the intermolecular/intramolecular interactions present in the studied structure (Figure 3. *a* - 3. *b*), the pair of bridged benzoates controls the stability of the dimeric complex. The Co^{II} ion is found in a deformed octahedral geometry caused by the variation in the (Co-O) bond lengths. The calculated (Co-O) bond lengths are in the range of 1.964-2.364 Å, not far from the experimental values range 2.0170(13)-2.2089(13) Å. The Cobalt (II) ion coordinates two nitrogen atoms in the apical positions. Experimental and theoretical (Co-N) bond lengths values show a good correlation. A remarkable difference is observed in the Co-O and Co-N chelating bond lengths values when comparing the neutral state with the first oxidized state: the bond lengths Co-O(1) and Co-O^i(4) decrease from 2.499 to 2.099 Å and 2.364 to 2.081Å, respectively (see Table 2). The calculated/experimental (Co…Co) distances are (4.764 / 4.518 Å). When increasing the oxidation order from the neutral to 3+ oxidized state, the bond angle O(4)#1-Co-O(1) increases from 144.8° to 163.1°, while O(3)-Co-O(1) and (O(1)-Co-O(2) angles decrease from 106.6° to 94.4° and from 121.5° to 114.4°, respectively, thismay indicate that the oxidation mechanism concerns the cobalt ions. The cobalt oxidation is confirmed by the decrease of the Co-O(1)

bond length value (from 2.499 Å to 2.047Å), and the increases in Co Hirshfeld atomic charge value from 0.169 e⁻ to 0.274 e⁻ with respect to the same oxidation order, whereas it decreases in the case of oxygen atom O(1) (from -0.260 e⁻ to -0.161 e⁻, see Table 4). This change in atomic charge and Co-O bond length could be explained by the donor mesomeric effect of the oxygen atom. The bond angle O(1)-Co-O(2) has a high angular tension (calc/exp: 58.7/60.63(5)°), which makes the links (Co-O) easy to be destroyed, while the opposite angle O(3)-Co-O(4)ⁱ is more stable (calc/exp: 108.60°/106.55(6)°). From these results, we notice that the metal ions lie in a deformed square plane. The angles O(2)-Co-N(2) and O(4)ⁱ-Co-N(1) with the values (calc/exp: 89.6/92.09(5)°) and (calc/exp: 89.6/ 90.14(5)°) respectively, confirm that all pyridine rings are perpendicular on the plane which contains the benzoate ligands. The dihedral angles (mentioned in SI) C(9)–O(4)–Co–O(5) = 358.9° and C(9)–O(2)–Co–O(54) = 178.5°, confirm the planarity of this part of the complex.

Energy and HOMO-LUMO Analysis

In the neutral state, the frontier molecular orbitals (FMOs), HOMO, and LUMO are mainly constituted by $Co-d_{z2}$ and $O-p_z$ orbitals, the concerned atoms are O (1), Oⁱ (1), O (4), and Oⁱ (4). HOMO-1 and HOMO-2 display a $Co-d_{xz}$ orbitals while the LUMO+1, LUMO+2 are located on the $N-p_z$, $C-p_z$ and $C-p_x$ orbitals of the pyridine rings and a low localization on the $Co-d_{x2-y2}$ orbitals. The HOMO-3 is made up by $Co-d_{x2-y2}$ and $O-p_y$ orbitals, while the LUMO+3 concerns $Co-d_{x2-y2}$ and $N-p_y$ orbitals. All the selected HOMOs and LUMOs in the complex $\left[Co_2\left(\mu_2\left(\eta_1-\eta_1\right)-Benz\right)_2\left(\mu_1-Benz\right)_2\left(Pyr\right)_4\right]^{1+}$ are centered on the cobalt ions d-orbitals and some of oxygen p-orbitals, the LUMO+3 excepted, which is centered on the pyridine rings (see-Figure S1). In the $\left[Co_2\left(\mu_2\left(\eta_1-\eta_1\right)-Benz\right)_2\left(\mu_1-Benz\right)_2\left(Pyr\right)_4\right]^{3+}$ the HOMO-1 and HOMO-3 are centered on the $Co-d_{xz}$ and $C-p_y$ orbitals of the (μ₂(η₁−η₁)–Benzoates. The HOMO is centered on the $C-p_y$ orbitals. However, the HOMO-2 is located on the (μ₂(η₁−η₁)–Benzoates, μ-Benzoates $C-p_y$ orbitals and the

$Co - d_{xy}$ orbitals (see-Figure S3). On the dicationic complex, the HOMO-1 and HOMO-2 are centered

on the bicoordinated benzoates $C - p_y$ orbitals. The HOMO-3 is centered also on the $C - p_y$ orbitals in

addition to the $Co - d_{yz}$ orbitals. The LUMO and LUMO+1 are localized on $O - p_z$, $Co - d_{x2-y2}$ orbitals,

while the LUMO+2 and LUMO+3 are mainly made by $Co - d_{z2}$ orbitals (see-Figure S2). As a

conclusion, in the studied compound, the lower energy gap that separates the occupied orbitals (HOMOs)

from the unoccupied orbitals (LUMOs) at the neutral, 1+, 2+ and 3+ oxidized states are 0.039 eV, 0.161

eV, 1.533 eV, and 0.013 eV respectively. This suggests a high chemical reactivity and low kinetic

stability. These values can explain the different eventual charge transfer interactions that take place within

the studied complex. The results of the orbital molecular boundaries analysis are shown in Table 3 and

Figure 4.

Table 3: Energy (E) and atomic percentage (%) of some molecular orbital (OMs) of the

$Co_2(\mu_2(\eta_1-\eta_1)-Benz)_2(\mu_1-Benz)_2(Pyr)_4$ calculated by the BLYP / TZP method. (where: **H**=HOMO and

L=LUMO)

Orbital	L+3	L+2	L+1	L	H	H-1	H-2	H-3
Energy (eV)	-1.748	-1.845	-1.884	-2.876	-2.915	-3.498	-3.590	-3.894
Co (%)	59.94	17.74	5.84	73.38	84.41	88.20	93.93	89.38
O (%)	9.95	3.41	0.00	4.89	9.57	5.11	1.24	3.62
N (%)	14.64	20.42	22.09	0.00	0.00	0.00	0.00	0.00
C (%)	2.37	50.51	60.87	0.00	0.00	0.00	0.00	0.00
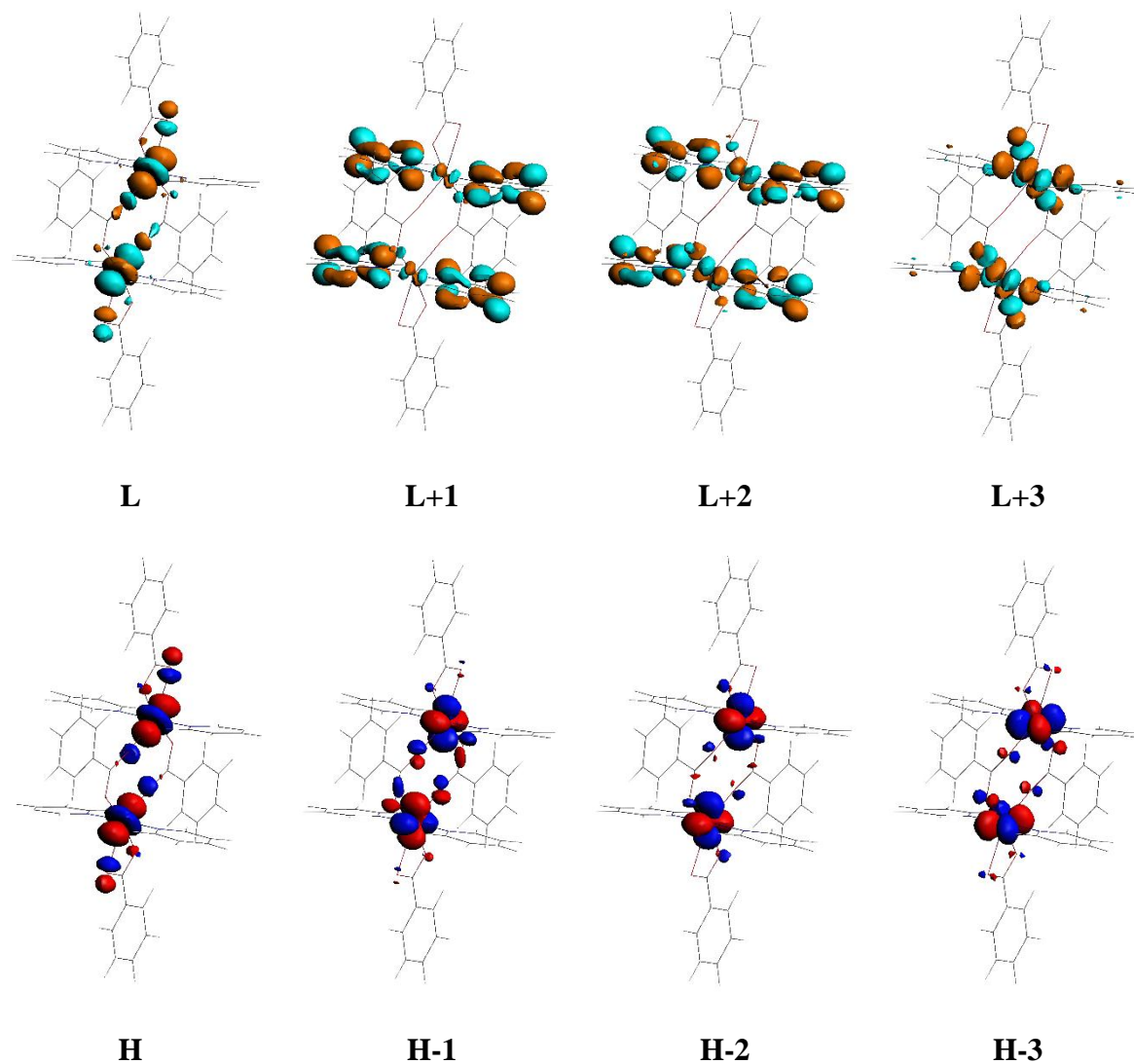
Figure 4: Schematic presentation of the frontier molecular orbitals of the complex

$Co_2(\mu_2(\eta_1-\eta_1)-Benz)_2(\mu_1-Benz)_2(Pyr)_4$.
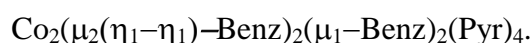
4.3. The Hirshfeld atomic charge analysis (HAC)

In a molecular system, the (HAC) [35]analysis enlighten some properties such as the polarizabilities of the bonds, electronic structures, molecular dipole moments, and the chemical reactivity. The Hirshfeld atomic charge of the title dimeric complex at different oxidized states are computed from the optimized structure, the results are summarized in Table 4. The HAC value of the cobalt (II) ions in the uncharged complex is 0.169 e⁻, it is barely varied when applying the formal charge (1+) and (2+) and it becomes 0.274 e⁻ at (3+) oxidized state. The atoms directly attached to the metal ion (Nitrogen and Oxygen) are

negatively charged, that shows the existence of an electrostatic attraction and donation effect of benzoate and pyridine ligands. So, the Cobalt-Nitrogen and Cobalt-Oxygen bonds suggest ionic contribution. The nitrogen HAC is unchanged at all the oxidation states, while those of oxygen atoms decrease as previously noticed. The results also indicate that the carbon atoms of bridging carboxylate C(8) are the poorest electron site with an atomic charge of about (0.172 e⁻). Coming after, the carbon C(1) of the μ_1−benzoate holds q = 0.166 e⁻. Their atomic charges increase with the oxidation state of the system C(1) from 0.166 to 0.200 e⁻, and C(8) from 0.172e⁻to 0.207 e⁻. All other carbon atomic charges C(20), C(19), C(15), and C(24) remain unchanged during oxidation.

Table 4: Hirshfeld charge analysis of the dimer complex at different oxidation states using BLYP functional and TZP basis set.

Oxidation state	(0)	(1+)	(2+)	(3+)
Atom				
Co	0.169	0.253	0.220	0.274
C(1)	0.166	0.178	0.197	0.200
O(1)	-0.260	-0.228	-0.160	-0.161
O(2)	-0.205	-0.188	-0.162	-0.166
C(8)	0.172	0.183	0.199	0.207
O^i(4)	-0.221	-0.216	-0.175	-0.164
O^i(3)	-0.198	-0.185	-0.172	-0.153
C(24)	0.045	0.050	0.051	0.051
C(20)	0.049	0.052	0.051	0.050
N(2)	-0.042	-0.044	-0.043	-0.046
C(15)	0.048	0.051	0.050	0.049
C(19)	0.044	0.049	0.049	0.050

N(1)	-0.042	-0.045	-0.042	-0.045
O(3)	-0.198	-0.185	-0.172	-0.153

4.4. AIM calculation: topological parameters at bond critical points (BCPs)

To understand the various intramolecular/intermolecular interactions in molecular systems which play an important role in crystal structures, a topological study was performed using Atoms in Molecules theory developed by Bader [36,37]. It provides a description of molecules and more particularly of their chemical bonds. This theory is based on the study of the electron density $\rho(r)$ and their Laplacian $\nabla^2\rho(r)$. A BCP represents the topological description of the interaction between pair of atoms. Furthermore, Espinosa et al. divided the atomic interaction into three categories according to the Potential energy $V(r)$, sign of the Total electron energy density H (r), and the Lagrangian kinetic energy G(r) [38–42]. The first class represents the pure covalent interaction (ρ (r) > 0.15, $\nabla^2\rho$ (r) < 0, H (r) < 0, | V | / G > 2). The second class is related to a pure closed-layer interaction conditioned by (ρ (r) < 0.07, $\nabla^2\rho$ (r) > 0, H (r) > 0, | V | / G < 1) and the third class corresponds to the intermediate interactions with (0.07 < ρ (r) < 0.15, $\nabla^2\rho$ (r) < 0, H (r) < 0, 1 < | V | / G < 2). Twelve BCP in each coordinate Covalent bond (Co-N and Co-O) and thirteen others referring to the intramolecular interactions were observed, Table S5 and Figure S4 (a, b). The ρ(BCPs) at cobalt bonds lie in the 0.03-0.1 (a.u.) range. The strong local depletion (Laplacian > 0) confirms an electrostatic interaction between cobalt and oxygen or nitrogen atoms of ligand. The bands Co-N(2), Co-N(1), Co-O(3), and Co-O(2) are more ionic than Co-O^i(4) and Co-O(1). We notice also the existence of two types of π---π interactions, the first one was founded between each pair of cis-pyridine rings, at BCP13 and BCP13* with pyridine---pyridine distances 5.054 Å. The second is localized between O(4) and O^i(4) atoms at the BCP14 crossed by the symmetric axis in (0.000, 0.000, 0.000), with O(4)---O^i(4) distance about 3.197 Å. Furthermore, the bond critical points studies along the C-H---O intermolecular paths show that the electron densities ρ(BCP) values are in 0.002-0.04 (a.u.) range and the Laplacian $\nabla^2\rho$(BCP) values are found in a 0.002-0.04 (a.u.) range. According to Rozas et al., it is a typical

21

range for H-bonding interactions [43]. In addition, the positive values of ρ(BCP) and $\nabla^2\rho$(BCP) are characteristics of weak H-Bonding interactions [44].

4.5. Bond Decomposition Energy analysis (BDE)

The Bond Dissociation Energy was evaluated for the present dimeric complexusing Ziegler-Rauk approach [30]. It allows the calculation of the binding energy of a molecular system and decomposes it into different interest chemical fragments. The procedure gives an insight into the nature of the bonds. We have considered three cases of fragments to calculate their binding energy to the central cobalt ions; the pyridine rings, the ($\mu_2(\eta_1-\eta_1)$–Benz), and the pair of bridged benzoates (μ_1–Benz). The total binding energy is divided into three terms, Orbital energy (ΔE_{orb}) which explains the interactions between occupied and vacant orbital, the repulsive Pauli's energy (ΔE_{pauli}) and Electrostatic energy (ΔE_{elsta}). The separation between the different contributions (Equation 1) gives an overview of the nature of the link [45].

$$BDE = \Delta E_{str} + \Delta E_{orb} = \Delta E_{elstat} + \Delta E_{Pauli} + \Delta E_{orb} \tag{1}$$

$\Delta E_{Pauli} + \Delta E_{orb}$ give the degree of covalence of the bonds. From the results shown in Table 5, the bonds $Co-N_{pyr}$ and $Co-O_{benz}$ have an ionic contribution, which confirms the results obtained from the Hirshfeld charge. The bond Co-($\mu_2(\eta_1-\eta_1)$–Benz) is more ionic than Co-(μ_1–Benz) bonds.

Table 5: Decomposition Energies (eV) of the bonds Metal-ligands in the studied complex, where: Pyr = Pyridine, $\mu_2(\eta_1-\eta_1)$–Benz = bidentate benzoate, and μ_1–Benz= bridged benzoate.

	BDE(eV)	Ionic(%)	Covalent (%)
Co- Pyr	+100.000	99	1
Co-$\mu_2(\eta_1-\eta_1)$–Benz)	+100.002	96	4
Co-(μ_1–Benz)	+197.818	92	8

4.6.   Non-Covalent Interaction(NCI Plot)

The (NCI plot) [46–48] has been presented in order to characterize the intramolecular interactions in the dimeric complex. According to the isosurfaces color code, red and yellow represent the repulsive and weak repulsive interactions respectively, while blue and green represent the attractive and weak attractive interactions, respectively. The general observation of the NCI plot index is presented in Figure 5.
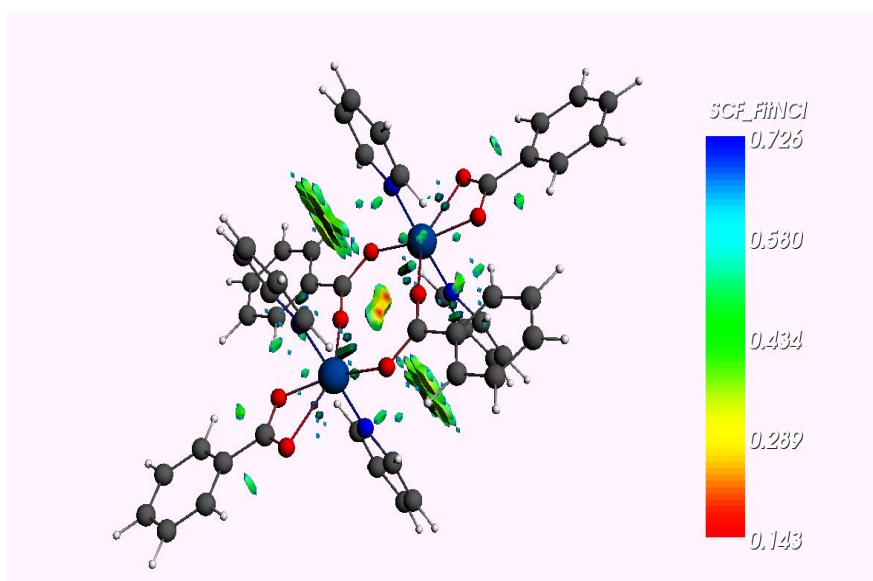

Figure 5: NCI surface of the assembly in the synthesized complex. The gradient cut-off is s =0.35 a.u, and the color scale is 0.143 <ρ< 0.726 au.

We notice that the weak attractive interactions are located between the -CH groups in the ortho-position of pyridine rings and benzoate oxygen atoms; ($O^i(4)$---H15-C(15), O(2)---H15-C(15), O(3)---H19-C(19), O(3)---H24-C(24), O(2)---H20-C(20), $O^i(4)$---H20-C(20), O(4)---H^i20-C^i20, $O^i(2)$ ---H^i20-C^i20, $O^i(3)$---H19-C19 and $O^i(2)$---H19-C(19). This type of interaction is also observed in (μ_1−Benz) which is represented by: ($O^i(4)$---H(10)-C(10) and O(4)---H(10)-C(10). The same type of interaction is observed in $\mu_2(\eta_1−\eta_1)$−Benz): (O(2)---H(7)-C(7), O(1)---H(3)-C(3), $O^i(1)$---$H^i(3)$-$C^i(3)$ and $O^i(2)$---$H^i(7)$-$C^i(3)$). Strong attractive π-π interactions are observed between cis-pyridine rings. Other interactions are

shown between the hydrogen atoms of μ_1–Benzoate and the oxygen of $\mu_2(\eta_1-\eta_1)$–Benz): $(O^i(2)$---H(10)-C(10) and O(2)---$H^i(10)$-$C^i(10))$ contact. The μ_1–Benzoate itself represents this type of interactions $(O^i(3)$---$H^i(14)$-$C^i(14)$ and O(3)---H(14)-C(14). The low intensity of repulsive interactions is observed only between $O^i(4)$ and O(4) $(O^i(4)$---O(4)). The NCI plot confirms the AIM results and suggests that the C-H$\cdots$O interactions control the stabilization of the assembly.

4.7. Molecular electrostatic potential (MEP) analysis

The electrostatic interactions (weak intermolecular and hydrogen bonding) have been evaluated using the same level of theory as the optimization. The 3D MEP surface provides the necessary information for the most reactive sites in the molecular system [49–53]. The electrostatic potential values at the surface are represented by five different colors, the color-coded surface indicates that the potential increase in order: red < orange < yellow < green < blue. The most negatively charged regions are characterized by red; it suggests the favored sites for a possible electrophilic attack. While, the most positive value which appears in dark blue, indicates the favored sites for a nucleophilic attack. The MEP values were calculated for the complex $Co_2(\mu_2(\eta_1-\eta_1)$–Benz$)_2(\mu_1$–Benz$)_2(Pyr)_4$using the following formula [31].

$$V\left(r\right) = \sum_{A} \frac{Z_A}{(R_A - r)} - \int \frac{\rho\left(r'\right)}{\left(r' - r\right)}\,dr' \qquad (2)$$

where V(**r**) represents the electrostatic molecular potential, Z_A is the charge of nucleus allocated at R_A. and ρ(**r'**) is the electron density function of the molecule and **r'** is the dummy integration variable. Figure 6 shows that the most negative potential is concentrated around the oxygen atoms, especially the O(1), and $O^i(1)$, which suggests the favored sites for a possible electrophilic attack. The green region is concentrated around the carbon atoms, it represents the neutral potential. The deepest green color is around the $C^i(8)$, C(8), C(1) and, $C^i(1)$, whereas the positive potentials are peripheral at the external H atoms of the ligand units. The MEP results prove the existence of H-bonding in agreement with AIM and NCI index studies (§ 4-4 and § 4-6).
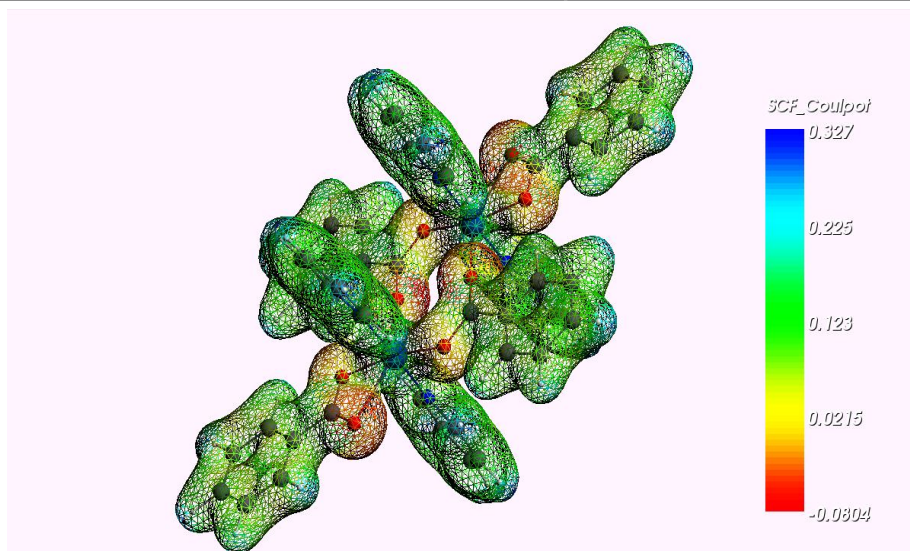
Figure 6: The 3D MEP surfaces of the complex at the neutral state calculated with DFT-BLYP method at TZP basis set.

4.8. Global reactivity descriptors

Electron affinity (A), Ionization potential (I), Electronegativity (χ), Chemical potential (μ), Chemical hardness (η), Chemical softness (S), and Electrophilicity index (ω) are known as the global reactivity descriptors. Their values are calculated from the frontier molecular orbitals energies (HOMO and LUMO). The calculations are investigated on the uncharged molecular structure $Co_2(\mu_2(\eta_1-\eta_1)-Benz)_2(\mu_1-Benz)_2(Pyr)_4$. According to Koopmans' theorem [31], the ionization potential (***I***) and electron affinity (***A***) can be donated by the following equations [34]:

$$I = -E_{HOMO} \qquad A = -E_{LUMO} \qquad (3)$$

The electronegativity (χ) index, the chemical potential (μ) and chemical hardness (η) are defined as [32,33]:

$$\chi = -\mu = -\frac{1}{2}\left(E_{LUMO} + E_{HOMO}\right) \qquad (4)$$

$$\mu = \frac{1}{2}\left(E_{LUMO} + E_{HOMO}\right) \qquad (5)$$

$$\eta = (E_{LUMO} - E_{HOMO}) \quad (6)$$

The chemical softness (S) is defined as the inverse of the global hardness (η):

$$S = 1/\eta \quad (7)$$

The global electrophilicity index (ω) as introduced by Parr et al. [34] are donated as:

$$\omega = {}^{2}/_{2} \quad (8)$$

From the results shown in Table 6, the high ionization energy (2.915 eV) and the negative value of the chemical potential (-2.895 eV) suggest the stability of the title compound which means that it will not decompose easily into its elements. The electrons of the complex present a low resistance to the deformation during the small perturbations ($\eta = 0.039$ eV). Low gap energy indicatesa high chemicalsoftness (S= 25.64 eV^{-1}) of the title compound, this proves its high chemical and biologicalreactivity. The very high value of the electrophilicity index (107.5 eV), suggests a good electrophilic character of the complex.

Table 6: Global reactivity descriptors of the $Co_2(\mu_2(\eta_1-\eta_1)-Benz)_2(\mu_1-Benz)_2(Pyr)_4$.

Parameters	Values
Ionization potential (I)	2.915
Electron affinity (A)	2.876
Electronegativity (χ)	2.895
Chemical potential (μ)	-2.895
Global chemical softness (S)	25.64

Global chemical hardness (η)	0.039
Electrophilicity index (ω)	107.5

*All values are given in (eV) with the exception of the global chemical softness S is given in (eV^{-1}).

4.9. Local reactivity descriptors

The most probable nucleophilic, electrophilic, or radical sites are investigated on the molecular structure. It leads to some reactivity indexes not accessible with other quantum methods, such as the Fukui functions which are given by:

$$f(r) = \left(\frac{\partial \rho(r)}{\partial N} \right)_{v(r)} \tag{9}$$

$\rho(r)$ is defined as the electronic density of the system and N their electrons number at the constant external potential v(r). These descriptors are often condensed on atomic values calculated using different approximations such as Hirshfeld [35], Mulliken [54], or natural orbital [55] by exploitation of the electronic population around an atom (k). Its importance lies in modeling the chemical reactivity and site selectivity [56,57]. In the aim of our study, they are given in terms of the variation of the Hirshfeld charges (q_i) of the atoms, which is accompanied by a change in the total number of electrons (N)in the dimeric complex, these can be written respectively as:

For electrophilic attack $\qquad f_k^+ = q_k(N+1) - q_k(N)$ $\qquad\qquad$ (10)

For nucleophilic attack $\qquad f_k^- = q_k(N) - q_k(N-1)$ $\qquad\qquad$ (11)

For radical attack $\qquad f_k^0 = 1/2(q_k(N+1) - q_k(N-1)$ $\qquad\qquad$ (12)

Where $q_k(N)$, $(q_k(N+1)$ and $q_k(N-1)$ are the electronic population of k atom in neutral, anionic, and cationic molecule respectively. Parr and Yang have shown that the atoms with higher values of the Fukui function (f_k) are more prone to reactivity under the corresponding types of attack. [58] The results shown

27

in Table S6 are carried out using single point calculations. They indicate that the Co^{II} ions (Co and Co^i) are the most reactive sites for the attacks of nucleophilic and free radical, followed by the oxygen atoms O(1) and $O^i(1)$. The hydrogen atoms H(6), H(11), H(12), H(13), $H^i(6)$, $H^i(11)$, $H^i(12)$, and $H^i(13)$ are very reactive to the radical attacks because the corresponding C-H bonding is weakened under the effect of the Hydrogen bonding. The carbon atoms C(2) and $C^i(2)$ are the most reactive sites prone to electrophilic attacks.

4.10. Infra-Red analysis

The experimental and the calculated IR spectra of the complex $Co_2(\mu_2(\eta_1-\eta_1)-Benz)_2(\mu_1-Benz)_2(Pyr)_4$ have been investigated. The theoretical vibrational frequencies were obtained by using the BLYP method and the TZP basis set. The corresponding spectra are shown in Figure 7.

4.10.1. C-O vibrations

The experimental IR spectrum exhibits a strong absorption band at $1215\,cm^{-1}$ which may be assigned to the stretching vibration mode of C-O bonds. It is found in the theoretical spectrum at wave number $1291\,cm^{-1}\,cm^{-1}$.

4.10.2. C-C, C=C vibrations

The experimental infrared spectrum shows absorption bands at 1444 and 1489 cm^{-1} attributed to the stretching vibrations mode of the aromatic C=C and C-C, respectively. In the calculated spectrum, they are observed at 1433 and $1476\,cm^{-1}$. The vibration predicted in the theoretical spectrum at $678\,cm^{-1}$ is identified as the aromatic C=C and C-C deformation modes. In the experimental spectrum, it is observed in 686 cm^{-1}.

4.10.3. -C=N- vibrations

The experimental infrared spectrum displays a band at 1570 cm^{-1} corresponding to the stretching vibration mode of the aromatic-C=N- It is absorbed in the calculated spectrum at 1576 cm^{-1}.

4.10.4. =C-N= vibrations

The experimental infrared spectrum reveals a band at 1398 cm^{-1} attributed to the stretching vibration mode of the aromatic =C-N=. It is observed in the calculated spectra at 1303 cm^{-1}.

4.10.5. C-H vibrations

The stretching vibration mode of the aromatic C-H bonds appears in the region 3039-3062 cm^{-1} cm^{-1}, which is observed in the calculated spectrum at 3076 cm^{-1} cm^{-1}. In-plane C-H bending vibrations were obtained in the range 1011-1050 cm^{-1} cm^{-1}, while the experimental range values are 1013-1073 cm^{-1} cm^{-1}. The absorption bands at 668, 680, 699, 702 andand 746 cm^{-1} $cm^{-1}$are due to the out-of-plane bending modes of C-H bonds in the calculated spectrum. In the experimental spectrum, they are detected at 702, 720, and 767 cm^{-1} .cm^{-1}.

4.10.6. Metal - Ligand vibrations

A weak band at 567 cm^{-1} cm^{-1}comes from the stretching vibration of the M-O linkage of the Co-O groups, while in our calculation this absorption band is found at 563 cm^{-1} cm^{-1}. The bending vibrations of Co-O are detected at 430 and 433 cm^{-1} cm^{-1} in the calculated and experimental IR spectra, respectively. The vibration band of the Co-N is found in the range of 641-643 cm^{-1} cm^{-1}, while the corresponding out-of-plane bending vibration is located at 468 cm^{-1} cm^{-1}. We have to mention that the band positioned at 3434 cm^{-1} cm^{-1} is assigned to the vibration of OH bonds of water compressed in the KBr pellet.

In conclusion, the experimental and theoretical data are complementary to each other. Indeed, the theoretical spectrum provides a help in the determination of the nature of the vibrations. The experimental and calculated values of the vibration frequencies are close in terms of position and intensity, attesting the well-known reliability of DFT at GGA level for the calculation of the vibrational spectra [59].
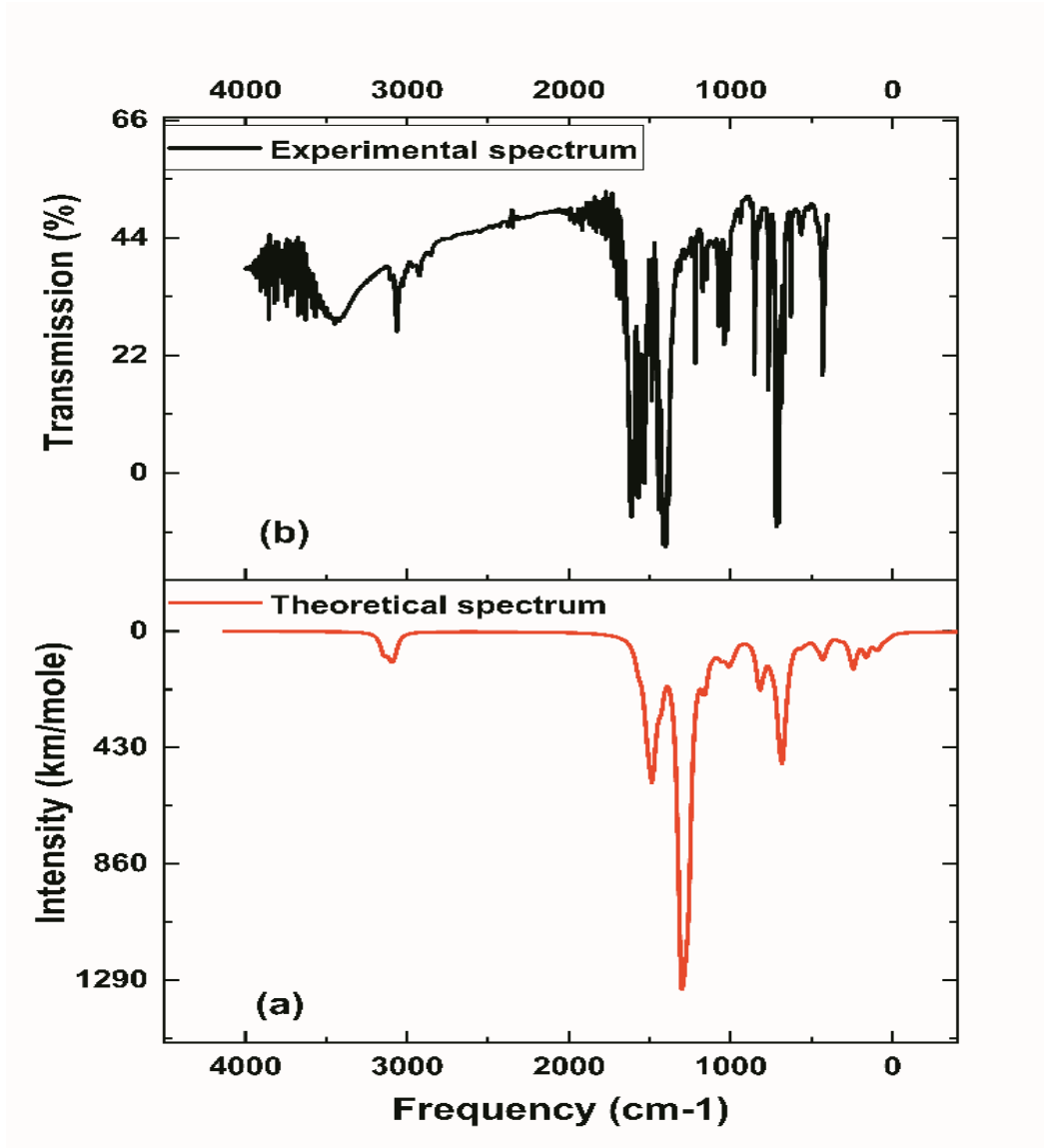
Figure 7: Fourier-transform infrared (FT-IR) spectra of the

$Co_2(\mu_2(\eta_1-\eta_1)-Benz)_2(\mu_1-Benz)_2(Pyr)_4$ complex. a) Theoretical spectrum, b) Experimental spectrum in

KBr pellet.

4.11. UV-Visible absorption

   The optical absorbance spectrum of this crystal was recorded at 298 K in the range of 190-800 nm in

DMSO as solvent (Figure 8). In the UV range [190-400 nm], the wavelengths 259.1 nm, 264.7 nm, 270

nm, and 277 nm may represent the π-π^* transitions of the benzoate and pyridine rings while the

absorption bands in the range [330-370nm], may refer the n-$\pi^*$of the benzoate ligands. However, the

visible spectrum recorded in the range of 400-800 nm reveals the absorption band at 552.4nm may due be to the d-d transition of the cobalt (II) ions.

For a deeper understanding of the experimental UV-Visible spectrum of the present complex; electronic transitions, electronic excitation energies, oscillating strength, major contributions, and their corresponding character have been investigated. The calculated UV-Visible spectra were performed using the Time-Dependent Density Functional Theory (TD-DFT) [27,60,61], employing the PBE gradient-corrected exchange-correlation functional of Perdew-Burke-Ernzerhof [62], the BLYP exchange-correlation functional by Becke [63], and Lee, Yang, and Parr [64], two well-established hybrid functionals (B3LYP [65], PBE0 [66]), the SAOP potential model [67] andthe range-separatedCAM-B3LYP [68], with the TZP basis set [24]. The experimental and theoretical electronic spectra in gas phase are given in Figure 8. The results are summarized in Table 7.
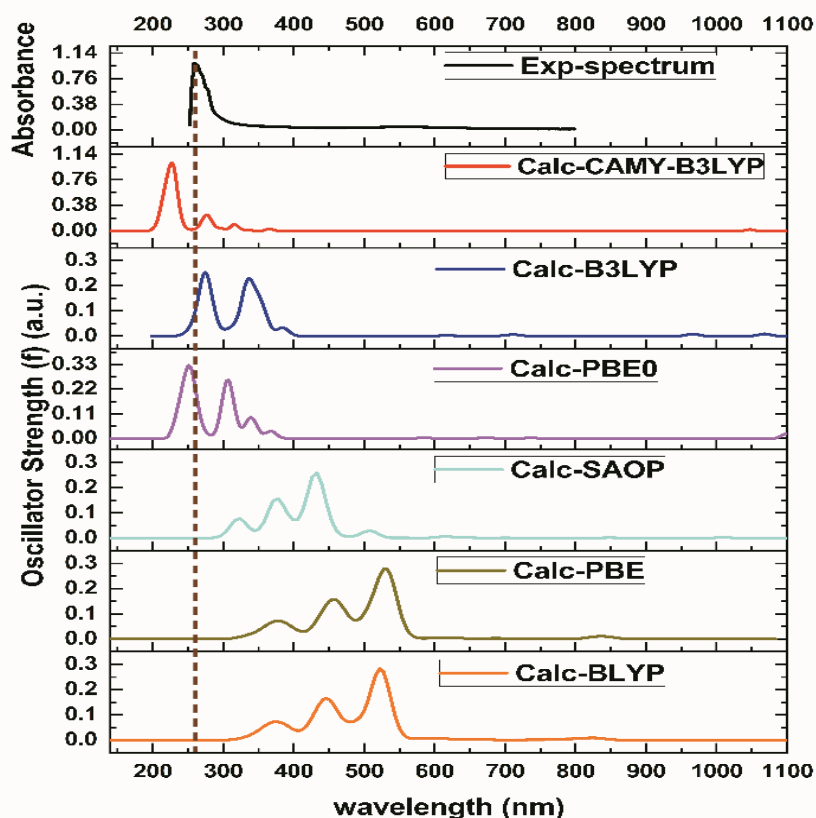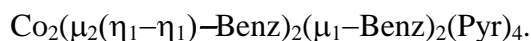
Figure 8: Experimental (Exp) and simulated (Calc) electronic UV-Vis spectra of

$Co_2(\mu_2(\eta_1-\eta_1)-Benz)_2(\mu_1-Benz)_2(Pyr)_4$.

The experimental and calculated wavelength spectra are almost similar in terms of the shape of the spectra, which, at theoretical level show three bands clearly visible with the hybrid functionals. Their relative intensity is, however, strongly dependent on the class of the functional (GGA, hybrid, range-separated). Moreover, the transitions are energetically strongly underestimated at the GGA level, as it is already pointed out in TD-DFT benchmarks of organic compounds [69–71], and also of a few metal complexes. [72–75] The theoretical spectrum is significantly improved when using the SOAP model potential developed by Baerends et al. [67], and even more with hybrid functionals (B3LYP, PBE0). This agrees with the good agreement found by Liao et al. in their study of iridium (III) complexes [76], and with the conclusions of Latouche et al. [72] who obtained the best agreement with the hybrid functionals, and even overestimated transitions with the range-separated functional for their Pt(II) or Ir(III) complexes. In our case, the range-separated functional CAM-B3LYP [68], as implemented in ADF with a Yukawa potential to separate the short/long ranges [77], (CAMY-B3LYP) delivers a spectrum which is also very close to the experimental one. Indeed, it could also deliver underestimated transition wavelengths, since the truncation of the experimental spectrum in the UV domain provides only a superior limit of the peak position.

All theoretical calculations indicate that three bands may be observed: the first one is a ML''CT Co $\rightarrow (\mu_1-Benz)$, the second band is MLCT Co $\rightarrow$ Pyr, the third one is L'MCT $(\mu_2(\eta_1-\eta_1)-Benz) \rightarrow$Co with some mixture of Co-d-d transition (see-Table S7). These theoretical bands show a large redshift in GGA spectra (BLYP and PBE) with respect to the experimental spectrum, their absorption bands at the level of these two methods are 387 nm, 460 nm, 552 nm for PBE, and 409 nm, 479 nm, 569nm for BLYP. The same bands are observed at smaller wavelength values: 373 nm, 402 nm, and 451 nm for SAOP model. The intensities of these absorption bands are ordered from smallest to largest. Further, the red shift with respect to experiment is reduced with hybrids PBE0 and B3LYP (PBE0 more reduced than B3LYP), the

corresponding absorption wavelengths are 258 nm, 315 nm, and 347 nm for PBE0. 286 nm, 346 nm, and 385nm for B3LYP, their intensities are in reverse order compared to the previous GGA band absorption values. With the CAM-B3LYP spectrum, the absorption bands are obtained at 226 nm, 281 nm, and 317 nm.

The maximum value of the oscillator strength is reached at the wavelength 226 nm (1.006 a.u.), representing the H-3$\rightarrow$ L+6 electronic transition with a Metal-Ligand-Charge-Transfer Co $\rightarrow$(μ_1−Benz). All the transitions are in the UV domain, possibly extended to the near purple. The bands from Co-d-d transitions are assumed to be hardly visible, their oscillator strength values are in the average of 0.0001 a.u$(f = 0.00074\,a.u.)$. Unfortunately, the limitation of the experimental spectrophotometer does not let access the bands at wavelengths smaller than 250 nm (vacuum UV).

Table 7: Selected optimized parameters for the complex $Co_2(\mu_2(\eta_1−\eta_1)$−Benz$)_2(\mu_1$−Benz$)_2(Pyr)_4$ in gas phase. The values λ_{calc} λ_{calc}, total energy, major contribution, the oscillator strength (f) and the electronic transition character are reported.

λ_{calc} [nm]	Energy (eV)	Oscillator Strength (f) (a.u.)	Major contributions		Character	
					B3LYP	
286	4.979	0.247	H-4$\rightarrow$L+6	(58.3%)	Co $\rightarrow$(μ_1−Benz)	(ML''CT)
			H-4$\rightarrow$L+10	(14.3%)	Co $\rightarrow$Pyr	(MLCT)
346	4.416	0.189	H-3$\rightarrow$L+2	(47.5%)	Co $\rightarrow$Pyr	(MLCT)
			H-4$\rightarrow$L+1	(37.9%)	Co $\rightarrow$Pyr	(MLCT)
			H-6$\rightarrow$L+1	(11.0%)	Co $\rightarrow$Pyr	(MLCT)
385	4.077	0.033	H-12$\rightarrow$L	(25.8%)	($\mu_2($ $\eta_1−\eta_1)$ −Benz)$\rightarrow$Co	(L'MCT)
			H-18$\rightarrow$L	(65.9%)	(μ_1−Benz) $\rightarrow$Co	
					CAMY- B3LYP	
226	7.455	1.006	H-3$\rightarrow$L+6	(24.0%)	Co $\rightarrow$(μ_1−Benz)	(ML''CT)

281	6.839	0.209	H-4→L+2	(39.5%)	Co →Pyr	(MLCT)
			H-3→L+1	(35.1%)	Co →Pyr	(MLCT)
317	6.180	0.094	H-18→L	(31.9%)	$(\mu_2(\eta_1-\eta_1)-Benz)\to Co$	(L'MCT)
PBE0						
258	5.596	0.325	H-5→L+5	(36.5%)	Co →(μ_1-Benz)	(ML''CT)
315	5.003	0.261	H-3→L+2	(44.7%)	Co →Pyr	(MLCT)
347	4.706	0.093	H-20→L	(51.4%)	$(\mu_2(\eta_1-\eta_1)-Benz)\to Co$	(L'MCT)
			H-7→L+5	(34.7%)	$(\mu_1-Benz)/(\mu_2(\eta_1-\eta_1)-Benz)\to Co$	(L'L''CT)
SAOP						
373	3.304	0.078	H-6→L+9	18.8%	Co →(μ_1-Benz)	(ML'CT)
			H-6→L+8	39.7%	Co→$(\mu_2(\eta_1-\eta_1)-Benz)$	(ML''CT)
			H-3→L+12	13.8%	Co →Pyr	(MLCT)
402	3.085	0.156	H-1→L+14	(99.9%)	Co →Pyr	(MLCT)
451	2.364	0.259	H-10→L	(66.0%)	$(\mu_2(\eta_1-\eta_1)-Benz)\to Co$	(L'MCT)
			H-3→L+3	(21.7%)	Co →Pyr	(MLCT)
PBE						
409	3.032	0.072	H-3→L+16	(91.8%)	Co →(μ_1-Benz)	(ML''CT)
479	2.582	0.157	H-3→L+14	(98.4%)	Co →Pyr	(MLCT)
569	2.170	0.279	H-7→L	(49.2%)	$(\mu_1-Benz)/(\mu_2(\eta_1-\eta_1)-Benz)\to Co$	(L''MCT) / (L'MCT)
			H→L+3	(19.7%)	Co→Co	(MC)
BLYP						
387	3.201	0.073	H-4→L+15	(99.9%)	Co →(μ_1-Benz)	(ML''CT)
460	2.685	0.165	H-4→L+12	(95.5%)	Co →Pyr	(MLCT)
552	2.176	0.283	H-7→L	(70.2%)	$(\mu_1-Benz)/(\mu_2(\eta_1-\eta_1)-Benz)\to Co$	(L''MCT) / (L'MCT)
			H-1→L+4	(17.6%)	Co →Pyr	(MLCT)

			H-2→L+5	(4.8%)	Co→Co	(MC)
			H-1→L+4	(2.9%)	Co→Co	(MC)
			H-5→L+6	(2.4%)	Co →Pyr	(MLCT)

Where **H**: HOMO, **L**: LUMO, **M**: Metal, **C**: Charge, **T**: Transfer, **L**: Pyr (Pyridine), **L'**: $\mu_2(\eta_1-\eta_1)$–Benz and **L''**: (μ_1–Benz)

4.12. Biological activities

4.12.1. Antimicrobial activity

The $Co_2(\mu_2(\eta_1-\eta_1)$–Benz$)_2(\mu_1$–Benz$)_2$(Pyr$)_4$complex was tested for its *in vitro* antimicrobial activity in the open conditions under visible/white light by the agar disk diffusion assay against six bacterial strains and one pathogenic fungi using different concentrations. The results of the antimicrobial activity are presented in Table 8 and are compared with gentamycin and penicillin as commercially available drugs.

Table 8: Results of the antimicrobial activity of $Co_2(\mu_2(\eta_1-\eta_1)$–Benz$)_2(\mu_1$–Benz$)_2$(Pyr$)_4$

Dilution (mg/mL)	Inhibition zone (mm)						
	E. coli ATCC 25922	*E. coli*	*K. pneumonae*	*S. aureus* ATCC 25923	*S. aureus*	*P. aeruginosa* ATCC 1117	*C. albicans* ATCC 90029
1	15 ± 0.3	10 ± 0.3	12 ± 0.3	10 ± 0.6	12 ± 0.1	8 ± 0.5	26 ± 0.1
0.5	9 ± 0.2	8 ± 0.1	8 ± 0.1	8 ± 0.3	9 ± 0.2	7 ± 0.3	20 ± 0.4
0.25	7 ± 0.5	-	-	8 ± 0.2	8 ± 0.3	-	15 ± 0.3
0.125	-		-	8 ± 0.5	-	-	11 ± 0.6
0.0625	-		-	-	-	-	9 ± 0.6
MIC(μg/mL)	125	250	250	62.5	125	250	31.25

Values expressed are means ± SD of three measurements ($p < 0.05$). (-) No zones of inhibition around the discs. MIC: the minimum inhibitory concentration

The tested complex was found to be active against all the tested strains. Indeed, the greatest zone of inhibition was observed against the fungi strain *C. Albicans* ATCC 90029 with a minimum inhibitory concentration value at 31.25 μg/mL. Moderate antibacterial activity was detected against all the tested bacterial strains with values of MIC ranging from 62.5 to 250 μg/mL.

Metal ion complexes are absorbed into the cell walls of microorganisms, which disrupt the respiratory processes of cells and thus prevent the synthesis of proteins necessary for the further growth of microorganisms. Consequently, the use of metal ion complexes as antimicrobial agents is essential for inhibiting microbial growth [78]. The results of antimicrobial activity could be explained by the good coordination of the metal ion with the chelating pyridine and benzoate ligands, resulting in the overlap of the ligand orbital and partial sharing of the positive charge of the ion with the donor groups, inducing a decrease in the polarity of the metal ion. Thus, itenhances the lipophilic character of the metal ion complex. This improves evidently the penetration of the complexes through the lipid membranes, leading to the deactivation of the bonding sites on enzymes of the microorganisms [79,80]. According to Kouris et al. [81], the presence of N-donor ligands like the pyridine groups and the chelating effects in the Co (II) complex may contribute to the enhancement of antimicrobial activity. Moreover, the important role of the benzoate group as a ligand in delivering complexes to bacterial cells may improve the antimicrobial effects [82].

4.12.2. Antioxidant activities

The antioxidant properties of the synthesized complex were evaluated using four different methods namely DPPH and H_2O_2 radical scavenging activities, total antioxidant capacity and ferric reducing antioxidant power. The tested complex and the reference molecules (BHA, BHT and ascorbic acid) showed antioxidant activity in all the tested systems and the results are illustrated in Table 9.

Table 9: Antioxidant properties of $Co_2(\mu_2(\eta_1-\eta_1)-Benz)_2(\mu_1-Benz)_2(Pyr)_4$

Extract and standards	DPPH assay[a] % of inhibition	H_2O_2 assay[a] % of inhibition	FRAP assay[a] µg EAA/mg	TAC assay [a] µg EAA/mg
Co complex	24.8 ± 0.55	65.78 ± 0.67	4.94 ± 0.01	29.23 ± 0.008
BHA[b]	98.08 ± 0,86	NT	NT	NT
BHT[b]	94.05 ± 0.9	NT	NT	NT

Ascorbic acid[b]	96.1 ± 0.18	62.32 ± 0.26	NT	NT

[a] Values expressed are means ± SD of three measurements ($p < 0.05$); [b] Reference compounds; NT: not tested.

The results of the antioxidant activity indicated the potent capacity of the tested complex to scavenge free radicals H_2O_2 with a percentage of inhibition at 65.78 ± 0.67% compared to ascorbic acid as reference. Moreover, a good antioxidant ability to reduce iron and molybdenum transition metals was observed in TAC and FRAP assays, with values of 29.23 ± 0.008 and 4.94 ± 0.01 µg EAA/mg, respectively. But, in the DPPH test, the Co (II)-complex exhibited a moderate antioxidant activity with a value of 24.8 ± 0.55 % at the concentration of 100 µg/mL, compared to BHA, BHT, and ascorbic acid as references.

The result of the FRAP test is in agreement with data from Jafari et al. [83], which indicated the high activity of the cobalt (II) complex to reduce iron III into iron II. In addition, Benhassine et al. [84] reported the moderate antioxidant activity of Co(II)-complex in DPPH assay which is consistent with the results of the present study.

Hydrogen peroxide is a molecular species, which is very important because of its capacity to penetrate biological membranes. This species reacts with metal ions like iron and copper via Fenton or Haber–Weiss reactions in the presence of $O_2^{\bullet-}$ to generate hydroxyl radicals in cells and can cause many toxic effects [85]. The powerful antioxidant activity of the tested complex in all most assays could be assigned to the presence of an open-shell electronic configuration in cobalt (II)-complex which exhibits a better antioxidant activity [86]. In fact, previous research reported that the complexation of 3d-transition metal with ligands facilitates electron transfer increasing the antioxidant activity of complexes [87]. In contrast, other researchers attributed the strong antioxidant activity of the Co (II)-complex to the nature of attached ligands [88–90]. It is very important to mention that the experimental results are in good agreement with the local reactivity parameters obtained by the DFT method, which indicate that the hydrogen atoms: $H(6)$, $H(11)$, $H(12)$, $H(13)$, $H^i(6)$, $H^i(11)$, $H^i(12)$, and $H^i(13)$ of the benzoate and pyridine rings, are very reactive sites for the attacks of free radicals.

4.12.3. Anti-inflammatory activity

The *in vitro* anti-inflammatory activity of di-µ-benzoato-bis [benzoatodipyridine-cobalt (II)] complex and diclofenac sodium as standard drug was evaluated by egg albumin denaturation test and the results were expressed as percentage of inhibition. The data revealed that the tested complex and standard drug prevent the denaturation of albumin in concentration dependent manner (Figure 9). Diclofenac showed the maximum percentage of inhibition (99.23%) at the concentration of 4 mg/mL. Moreover, at the same concentration the tested complex exhibited a moderate anti-inflammatory effect with a percentage of inhibition at 11.48 %. The moderate anti-inflammatory activity of cobalt (II)-complex could be attributed to the interactions between the active centers in the tested complex with the aliphatic region around the lysine residue on the albumin protein [91].
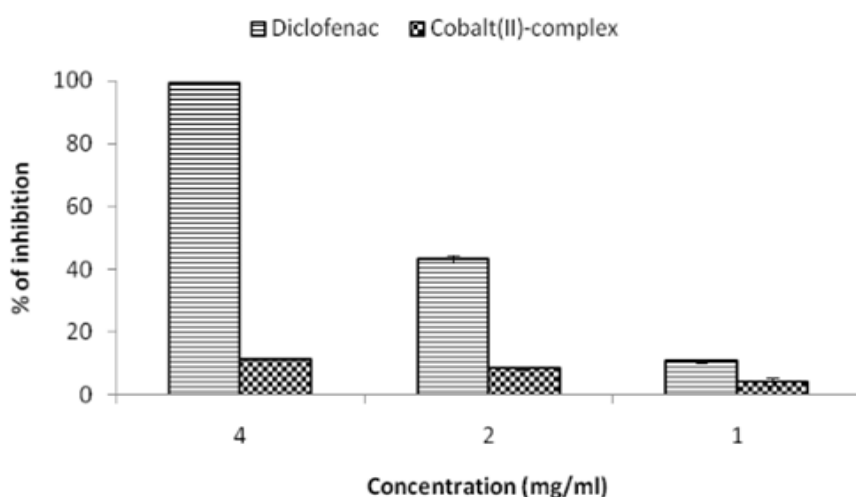

Figure 9: *In vitro* anti-inflammatory effect of Co (II) complex.

4.13. Thermogravimetric analysis (TG-DTA)

The thermal decomposition characteristics of the present complex have been investigated in the range of temperature [35-350°C], using thermal analytical techniques (TGA and DTA) under argon. The results are collected in Table 10. The TG-thermogram (Figure 10) shows three steps of decomposition. Generally, the decomposition in TGA analysis comes via partial loss of the organic moiety. The Co-N bonds are less stable than the Co-O bonds. It is explained by the mesomeric effect of oxygen atoms.

The title complex is thermally stable up to 107.7 °C. Above this temperature, comes the first step of the decomposition with weight loss of 22.87 % (4.848 mg), accompanied by an endothermic peak at 163.9 °C. It is stable up to 140.8 °C on the DTA thermogram, which reasonably accounted for the loss of four pyridine ligands (C_5H_5N), according to BDE analysis which shows that the Co-N connection is more ionic than Co-O. The second stage was detected at 177.8-248.3°C intervals, displaying a weight loss of 10.89% (2.309 mg). Two successively endothermic peaks are shown on the DTA thermogram at 232.5 and 243.5 °C may due to the removal of two bidentate benzoate $((\mu_2(\eta_1-\eta_1)-Benz))$ and two bridged benzoates (μ_1-Benz) respectively; this is explained by the angular force of the $(\mu_2(\eta_1-\eta_1)-Benzoate)$ which presents less stability than the bridged once. The DTA thermogram exhibits a final endothermic peak at 269.3 °C corresponding to the melting point
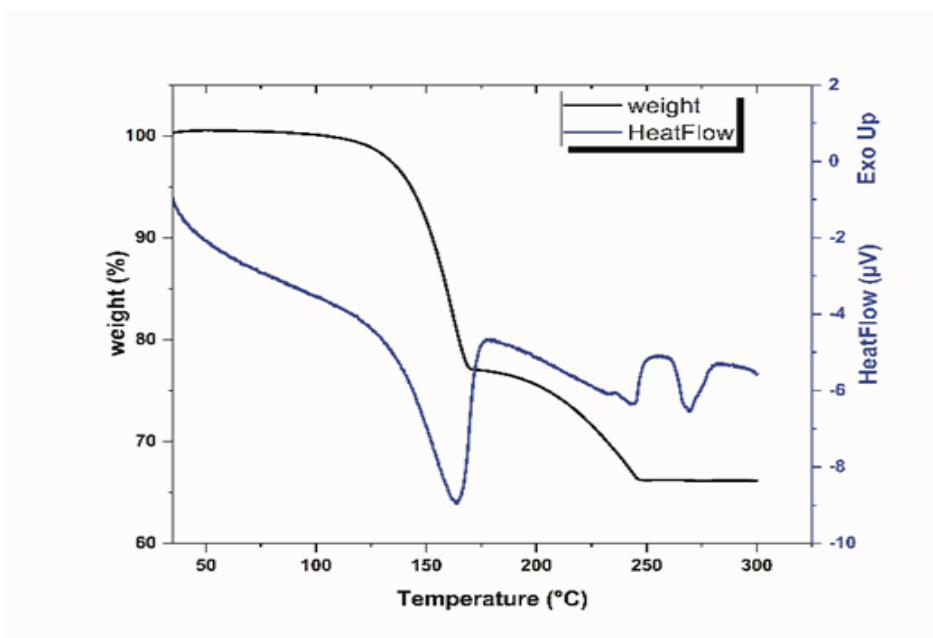

Figure 10: TG-DTA curves of the dimeric cobalt complex, sample mass 21.2 mg, heating rate 10°C min^{-1}, atmosphere: argon.

Table 10: Thermal results TG-DTA of $Co_2(\mu_2(\eta_1-\eta_1)-Benz)_2(\mu_1-Benz)_2(Pyr)_4$

	TG T°$_{range}$/°C	DTA T$_{max\cdot peaks}$/°C	Peak nature	Mass loss %(mg)	Decomposition assignment	Residual %(mg)

Stage (I)	107-170	163.9	Endo	22.87 (4.848)	4(Pyr)	66.24
Stage (II)	178-248		Endo	10.89 (2.309)	2(μ_2($\eta_1-\eta_1$) –Benz) 2(μ_1–Benz)	(14.043)
Stage (III)	---	269.3	Endo	0.00	---	

Process under argon atmosphere, the residual mass was measured at 300 °C

5. Conclusion

In this paper, the complex $Co_2(\mu_2(\eta_1-\eta_1)-Benz)_2(\mu_1-Benz)_2(Pyr)_4$ $[Co_2(\mu-Benz)_2(Benz)_2(Pyr)_4]$ has been synthesized and characterized. X-ray crystallographic analysis revealed that pair of cobalt (II) ions are coordinated by two bridged benzoate ligands, each cobalt has two pyridine rings and $(\mu_2(\eta_1-\eta_1)-$Benzoate with (O-Co-O) band angle of about 60°. The synthesized compound has been characterized by different spectroscopic and analytical techniques such as UV-Visible analysis, FT-IR and Thermal analysis (TG and DTA). Density Functional Theory (DFT) calculations were used to achieve more details and accuracy in the assignment of the experimental data, also to explain some physical and chemical properties such as the band gaps of materials, the energies of dissociating molecular, the origin of the electronic transitions in UV-Vis absorption spectrum, the intermolecular/ intramolecular interactions and the chemical reactivity. The optimized molecular geometry shows that the Co (II) ions coordinated in a slightly distorted octahedral environment, where the (Co-O) bond length variations are in 2.031-2.209 Å range. All the donating sites are almost in the same plane, the pyridine rings are in apical octahedral positions. The Hirshfeld atomic charges analysis suggests that the highest concentration of the negative charge is located around the oxygen atoms especially O(1), while the Co atom, C(8), and C(1) have the highest electronic deficit; they are the most prone to a nucleophilic attack. This is in good agreement with the features of a MEP plot. The calculated band gaps suggest a high chemical reactivity and low kinetic stability of the complex at different oxidation states; the dicationic state is founded slightly more stable than the other oxidation states. The studied molecular structure shows many types of intramolecular / intermolecular, attractive and repulsive interactions. They were investigated using the

NCI plot and AIM analysis; π-π interactions located between cis-pyridine rings are founded. All of these interactions control the stability of the complex. The bond dissociation energies results mention that all cobalt ion-ligand bands have ionic contributions. Moreover, the electronic spectrum provided assignments for characteristic absorption bands. Good agreement between the experimental and the calculated frequencies has been observed. The thermal analysis revealed that the complex is thermally stable up to 107.7 °C. However, the melting point is at 269.3 °C. Furthermore, the present investigation indicates interesting *in vitro* biological activities. Indeed, it can be concluded that the tested complex could be used as a good agent with antioxidant properties against pathological damage due to free radicals inducing inflammations and infectious diseases. Moreover, the results of the antimicrobial activity encourage *in silico*/docking study of this metal complex with microbial genomes. This could give better insight into metal-genome interactions at the molecular level.

Author Contributions

OK executed the research, optimized methods and participated in conceptualizing the study, drafting and revising the manuscript; NB conceived the study, wrote the manuscript and supervised the study; SZ participated in conducting the study, entering data and drafting the manuscript. SM participated in conducting the biological investigation, collecting and entering biological data and revising the manuscript; SG solved and refined the crystallographic data and performed the experimental structural analysis; AG revised the manuscript, HH conceptualized and designed the study, analyzed data, drafted and revised the manuscript; and HC participated in conducting the investigation, entering data and drafting the manuscript All authors read and approved the final manuscript submission.

Declaration of Competing Interest

The authors declare that they have no known competing financial interests or personal relationships that could have appeared to influence the work reported in this paper.

Acknowledgements

Supplementary data

Supplementary data to this article can be found online at

Author statment

OK executed the research, optimized methods and participated in conceptualizing the study, drafting and revising the manuscript; NB conceived the study, wrote the manuscript and supervised the study; SZ participated in conducting the study, entering data and drafting the manuscript. SM participated in conducting the biological investigation, collecting and entering biological data and revising the manuscript; SG solved and refined the crystallographic data and performed the experimental structural analysis; AG revised the manuscript, HH conceptualized and designed the study, analyzed data, drafted and revised the manuscript; and HC participated in conducting the investigation, entering data and drafting the manuscript All authors read and approved the final manuscript submission.

References

[1]   M. Pajak, M. WoŹniczka, A. Vogt, A. Kufelnicki, Reversible uptake of molecular oxygen by heteroligandCo(II)–l-α-amino acid–imidazole systems: equilibrium models at full mass balance, Chemistry Central Journal. 11 (2017) 90.

[2]   N. Benbellat, K.S. Gavrilenko, Y. le Gal, O. Cador, S. Golhen, A. Gouasmia, J.M. Fabre, L. Ouahab, Co(II)-Co(II) paddlewheel complex with a redox-active ligand derived from TTF., Inorganic Chemistry. 45 (2006) 10440–10442.

[3]   N. Benbellat, Y. le Gal, S. Golhen, A. Gouasmia, L. Ouahab, Synthesis, characterization and X-ray structures of tetrathiafulvalene-type electron donors bearing one pyridine group, Synthetic Metals. 162 (2012) 1789–1797.

[4]   J.F. Wang, R.Y. Li, P. Li, W.K. Dong, Exploring coordination behaviors, structural characterizations and theoretical calculations of structurally different Cu(II), Co(II) and Ni(II) emissive complexes constructed from a salamo-based ligand and 4,4'-bipy, InorganicaChimica Acta. 518 (2021) 120247.

[5]   S. NasiriSovari, F. Zobi, Recent Studies on the Antimicrobial Activity of Transition Metal Complexes of Groups 6–12, Chemistry (Easton). 2 (2020) 418–452.

[6]   A.A. García-Valdivia, F. Jannus, A. García-García, D. Choquesillo-Lazarte, B. Fernández, M. Medina-O'donnell, J.A. Lupiáñez, J. Cepeda, F.J. Reyes-Zurita, A. Rodríguez-Diéguez, Anti-cancer and anti-inflammatory activities of a new family of coordination compounds based on divalent transition metal ions and indazole-3-carboxylic acid, Journal of Inorganic Biochemistry. 215 (2021) 111308.

[7]   S. Talebi, V. Amani, M. Saber-Tehrani, A. Abedi, Improvement of the Biological Activity of a New Cobalt(III) Complex through Loading into a Nanocarrier, and the Characterization Thereof, ChemistrySelect. 4 (2019) 13235–13240.

[8]   L. Yang, D.C. Crans, S.M. Miller, A. la Cour, O.P. Anderson, P.M. Kaszynski, M.E. Godzala, L.T.D. Austin, G.R. Willsky, Cobalt(II) and cobalt(III) dipicolinate complexes: Solid state, solution, and in vivo insulin-like properties, Inorganic Chemistry. 41 (2002) 4859–4871.

[9]   M. Manjunatha, V. Srinivasan, S. HaseenBuvabi, Biological studies of novel 22-Membered N2O2 diazadioxa Macrocyclic Bis-Triazoles transition metal Complexes: Synthesis and physicochemical studies, Materials Today: Proceedings. 47 (2021) 4538–4547.

[10]   X. Fan, J. Dong, R. Min, Y. Chen, X. Yi, J. Zhou, S. Zhang, Cobalt(II) complexes with thiosemicarbazone as potential antitumor agents: Synthesis, crystal structures, DNA interactions, and cytotoxicity, Journal of Coordination Chemistry. 66 (2013) 4268–4279.

[11]   G. Wei, N. Lin, Y. Gu, X. Ren, G. Zhao, S. Guang, J. Feng, H. Xu, High selectivity improvement of chemosensors through hydrogen-induced emission (HIE) for detection of Hg2+ in vivo and in vitro, Sensors and Actuators B: Chemical. 321 (2020) 128532.

[12]   M. Claudel, J. v. Schwarte, K.M. Fromm, New Antimicrobial Strategies Based on Metal Complexes, Chemistry (Easton). 2 (2020) 849–899.

[13]   Y. R. Li, Z. Jia, M. Trush, Defining ROS in Biology and Medicine, Reactive Oxygen Species. 1 (2016) 9–21.

[14]   A. Phaniendra, D.B. Jestadi, L. Periyasamy, Free Radicals: Properties, Sources, Targets, and Their Implication in Various Diseases, Indian Journal of Clinical Biochemistry. 30 (2015) 11–26.

[15]   D. Hannachi, N. el HoudaAmrane, L. Merzoud, H. Chermette, Exploring the antioxidant activity of thiaflavan compounds: a quantum chemical study, New Journal of Chemistry. 45 (2021) 13451–13462.

[16]   A. Altomare, M. C. Burla, M. Camalli, G. L. Cascarano, C. Giacovazzo, A. Guagliardi, A. G. G. Moliterni, G. Polidori, R. Spagna, SIR97: a new tool for crystal structure determination and refinement, J ApplCrystallogr. 32 (1999) 115–119.

[17]   G. M. Sheldrick, IUCr, A short history of SHELX, Acta Crystallogr. 64 (2007) 112–122.

[18]   L. J. Farrugia, IUCr, WinGX and ORTEP for Windows: an update, J ApplCrystallogr. 45 (2012) 849–854.

[19]   C. Mouffouk, L. Hambaba, H. Haba, S. Mouffouk, C. Bensouici, Evaluation of Cytotoxic Effect, Anti-Cholinesterase, Hemolytic and Antibacterial activities of the Species Scabiosastellata L., Current Bioactive Compounds. 16 (2018) 72–79.

[20]   S. Mouffouk, L. Marcourt, M. Benkhaled, K. Boudiaf, J. L. Wolfender, H. Haba, Two New Prenylated Isoflavonoids from Erinaceaanthyllis with Antioxidant and Antibacterial Activities, Natural Product Communications. 12 (2017) 1065–1068.

[21]   R.J. Ruch, S. jun Cheng, J.E. Klaunig, Prevention of cytotoxicity and inhibition of intercellular communication by antioxidant catechins isolated from Chinese green tea, Carcinogenesis. 10 (1989) 1003–1008.

[22]   M. S. Blois, Antioxidant Determinations by the Use of a Stable Free Radical, Nature. 181 (1958) 1199–1200.

[23] D. Sunmathi, R. Sivakumar, K. Ravikumar, In vitro Anti-inflammatory and Antiarthritic activity of ethanolic leaf extract of Alternanthera sessilis (L.) R.BR. ex DC and Alternanthera philoxeroides (Mart.)Griseb, INTERNATIONAL JOURNAL OF ADVANCES IN PHARMACY, BIOLOGY AND CHEMISTRY. 5(2) (2016) 2277–4688.

[24] E. J. Baerends, T. Ziegler, A. J. Atkins, J. Autschbach, D. Bashford, A. Bérces, F. M. Bickelhaupt, C. Bo, P. M. Boerrigter, L. Cavallo, D. P. Chong, D. V. Chulhai, L. Deng, R. M. Dickson, J. M. Dieterich, D. E. Ellis, M. van Faassen, L. Fan, T. H. Fischer, C. Fonseca Guerra, M. Franchini, A. Ghysels, A. Giammona, S. J. A. van Gisbergen, A. W. Götz, J. A. Groeneveld, O. V. Gritsenko, M. Grüning, S. Gusarov, F. E. Harris, P. van den Hoek, C. R. Jacob, H. Jacobsen, L. Jensen, J. W. Kaminski, G. van Kessel, F. Kootstra, A. Kovalenko, M. V. Krykunov, E. van Lenthe, D. A. McCormack, A. Michalak, M. Mitoraj, S. M. Morton, J. Neugebauer, v. P. Nicu, L. Noodleman, v. P. Osinga, S. Patchkovskii, M. Pavanello, C. A. Peeples, P. H. T. Philipsen, D. Post, C. C. Pye, W. Ravenek, J. I. Rodriguez, P. Ros, R. Rüger, P. R. T. Schipper, H. van Schoot, G. Schreckenbach, J. S. Seldenthuis, M. Seth, J. G. Snijders, M. Solà, M. Swart, D. Swerhone, G. te Velde, P. Vernooijs, L. Versluis, L. Visscher, O. Visser, F. Wang, T. A.Wesolowski, E. M. van Wezenbeek, G. Wiesenekker, S. K. Wolff, T. K. Woo, A. L. Yakovlev, ADF2016.01, ADF2016.01, SCM, Theoretical Chemistry, Vrije Universiteit, Amsterdam, The Netherlands, 2016, Http://Www.Scm.Com. (n.d.).

[25] A.D. Becke, Density-functional exchange-energy approximation with correct asymptotic behavior, Physical Review A. 38 (1988) 3098–3100.

[26] C. Lee, W. Yang, R.G. Parr, Development of the Colle-Salvetti correlation-energy formula into a functional of the electron density, Phys Rev B Condens Matter. 37 (1988) 785–789. https://doi.org/10.1103/PHYSREVB.37.785.

[27] G. Scalmani, M. J. Frisch, B. Mennucci, J. Tomasi, R. Cammi, v. Barone, Geometries and properties of excited states in the gas phase and in solution: Theory and application of a time-dependent density functional theory polarizable continuum model, Journal of Chemical Physics. 124 (2006) 094107.

[28] M. Kohout, DGrid, DGrid, Version 4.3, Radebeul. (n.d.).

[29] Chemcraft - graphical software for visualization of quantum chemistry computations. https://www.chemcraftprog.com, Chemcraft - Graphical Software for Visualization of Quantum Chemistry Computations. Https://Www.Chemcraftprog.Com. (n.d.).

[30] T. Ziegler, A. Rauk, On the calculation of bonding energies by the HartreeFock Slater method, TheorChim Acta. 46 (1977) 1–10.

[31] T. Koopmans, T. Koopmans, Über die Zuordnung von Wellenfunktionen und Eigenwertenzu den EinzelnenElektronenEines Atoms, Physica. 1 (1934) 104–113.

[32] R. G. Parr, R. A. Donnelly, M. Levy, W. E. Palke, Electronegativity: The density functional viewpoint, The Journal of Chemical Physics. 68 (2008) 3801.

[33] R.G. Parr, L. v. Szentpály, S. Liu, Electrophilicity Index, J Am Chem Soc. 121 (1999) 1922–1924.

[34] H. Chermette, Chemical reactivity indexes in density functional theory, Journal of Computational Chemistry. 20 (1999) 129–154.

[35] F. L. Hirshfeld, Bonded-atom fragments for describing molecular charge densities, TheorChim Acta. 44 (1977) 129–138.

[36] v. Tognetti, L. Joubert, Density functional theory and Bader's atoms-in-molecules theory: towards a vivid dialogue, Physical Chemistry Chemical Physics. 16 (2014) 14539–14550.

[37] R. F. W. Bader, H. Essén, The characterization of atomic interactions, The Journal of Chemical Physics. 80 (1983) 1943–1960.

[38] E. Espinosa, I. Alkorta, J. Elguero, E. Molins, From weak to strong interactions: A comprehensive analysis of the topological and energetic properties of the electron density distribution involving X–H⋯F–Y systems, The Journal of Chemical Physics. 117 (2002) 5529.

[39] A.N. Egorova, V.G. Tsirel'son, , Electron distribution and chemical bonding in M3(XO4)2 molecules (M = Mg, Cu; X = P, V) as determined by Ab initio calculations, Russian Journal of Inorganic Chemistry. 51 (2006) 941–948.

[40] D. Marabello, R. Bianchi, G. Gervasio, F. Cargnoni, An experimental (120 K) and theoretical electron-density study of KMnO 4 and KClO4, Acta Crystallographica Section A: Foundations of Crystallography. 60 (2004) 494–501.

[41] C. Bo, M. Costas, J.M. Poblet, M.M. Rohmer, M. Benard, Electronic Structure of Rh2(μ-CO)(CO)2(H2PCH2PH2)2. An Example of a Non-A-Frame Structure, Inorganic Chemistry. 35 (1996) 3298–3306.

[42] I. Rozas, I. Alkorta, J. Elguero, ,Behavior of ylides containing N, O, and C atoms as hydrogen bond acceptors, J Am Chem Soc. 122 (2000) 11154–11161.

[43] S. Trabelsi, N. Issaoui, S.A. Brandán, F. Bardak, T. Roisnel, A. Atac, H. Marouani, Synthesis and physic-chemical properties of a novel chromate compound with potential biological applications, bis(2-phenylethylammonium) chromate(VI), Journal of Molecular Structure. 1185 (2019) 168–182.

[44] P. Su, Z. Chen, W. Wu, An energy decomposition analysis study for intramolecular non-covalent interaction, Chemical Physics Letters. 635 (2015) 250–256.

[45] T. Lu, F. Chen, Quantitative analysis of molecular surface based on improved Marching Tetrahedra algorithm, , Journal of Molecular Graphics and Modelling. 38 (2012) 314–323.

[46] E. Scrocco, J. Tomasi, Electronic Molecular Structure, Reactivity and Intermolecular Forces: An Euristic Interpretation by Means of Electrostatic Molecular Potentials, Advances in Quantum Chemistry. 11 (1978) 115–193.

[47] J. Andres, S. Berski, J. Contreras-Garcia, P. Gonzalez-Navarrete, Following the molecular mechanism for the NH3+ LiH→ LiNH2+ H2 chemical reaction: a study based on the joint use of the quantum theory of atoms in molecules (QTAIM) and noncovalent interaction (NCI) index, The Journal of Physical Chemistry A. 118 (2014) 1663–1672.

[48] E. R. Johnson, S. Keinan, P. Mori-Sánchez, J. Contreras-García, A. J. Cohen, W. Yang, Revealing Noncovalent Interactions, Journal of the American Chemical Society. 132 (2010) 6498–6506.

[49] P Politzer, P R Laurence, K Jayasuriya, Molecular electrostatic potentials: an effective tool for the elucidation of biochemical phenomena, Environ Health Perspect. 61 (1985) 191–202.

[50] J. S. Murray, P. Politzer, The electrostatic potential: an overview, Wiley Interdisciplinary Reviews: Computational Molecular Science. 1 (2011) 153–163.

[51] S. R. Gadre, C. H. Suresh, N. Mohan, Electrostatic Potential Topology for Probing Molecular Structure, Bonding and Reactivity, Molecules. 26 (2021) 3289.

[52] S. Lakshminarayanan, v. Jeyasingh, K. Murugesan, N. Selvapalam, G. Dass, Molecular electrostatic potential (MEP) surface analysis of chemo sensors: An extra supporting hand for strength, selectivity & non-traditional interactions, Journal of Photochemistry and Photobiology. 6 (2021) 100022.

[53] J. M. Campanario, E. Bronchalo, M. A. Hidalgo, An effective approach for teaching intermolecular interactions, J Chem Educ. 71 (1994) 761.

[54] R.S. Mulliken, Electronic Population Analysis on LCAO–MO Molecular Wave Functions. I, The Journal of Chemical Physics. 23 (2004) 1833.

[55] A.E. Reed, F. Weinhold, Natural bond orbital analysis of near-Hartree–Fock water dimer, The Journal of Chemical Physics. 78 (1988) 4066.

[56] R.G. Parr, W. Yang, Density functional approach to the frontier-electron theory of chemical reactivity, J Am Chem Soc. 106 (2002) 4049–4050.

[57] K. Fukui, Role of frontier orbitals in chemical reactions, Science (1979). 218 (1982) 747–754.

[58] W. Yang, W.J. Mortier, The use of global and local molecular parameters for the analysis of the gas-phase basicity of amines , J Am Chem Soc. 108 (2002) 5708–5711.

[59] H. Chermette, Density functional theory: A powerful tool for theoretical studies in coordination chemistry, Coordination Chemistry Reviews. 178–180 (1998) 699–721.

[60] M.E. Casida, H. Chermette, D. Jacquemin, Time-dependent density-functional theory for molecules and molecular solids, Journal of Molecular Structure: THEOCHEM. 914 (2009) 1–2.

[61] M.E. Casida, Time-dependent density-functional theory for molecules and molecular solids, Journal of Molecular Structure: THEOCHEM. 914 (2009) 3–18.

[62] J.P. Perdew, K. Burke, M. Ernzerhof, Generalized Gradient Approximation Made Simple , Physical Review Letters. 78 (1997) 1396.

[63] A.D. Becke, Density-functional exchange-energy approximation with correct asymptotic behavior, Physical Review A. 38 (1988) 3098.

[64] C. Lee, W. Yang, R.G. Parr, Development of the Colle-Salvetti correlation-energy formula into a functional of the electron density, Physical Review B. 37 (1988) 785.

[65] A. D. Becke, Density-functional thermochemistry. III. The role of exact exchange, The Journal of Chemical Physics. 98 (1993) 5648–5652.

[66] C. Adamo, v. Barone, Toward reliable density functional methods without adjustable parameters: The PBE0 model, The Journal of Chemical Physics. 110 (1999) 6158.

[67] O.V. Gritsenko, P.R.T. Schipper, E.J. Baerends, Ensuring proper short-range and asymptotic behavior of the exchange-correlation Kohn-Sham potential by modeling with a statistical average of different orbital model potentials, International Journal of Quantum Chemistry. 76 (2000) 407–419.

[68] T. Yanai, D. P. Tew, N. C. Handy, A new hybrid exchange–correlation functional using the Coulomb-attenuating method (CAM-B3LYP), Chemical Physics Letters. 393 (2004) 51–57.

[69] A. Stoliaroff, J. Rio, C. Latouche, Accurate computations to simulate the phosphorescence spectra of large transition complexes: simulated colors match experiment, New Journal of Chemistry. 43 (2019) 11903–11911.

[70] A. Stoliaroff, C. Latouche, Accurate Ab Initio Calculations on Various PV-Based Materials: Which Functional to Be Used?, Journal of Physical Chemistry C. 124 (2020) 8467–8478.

[71] C. Latouche, D. Skouteris, F. Palazzetti, v. Barone, TD-DFT benchmark on inorganic Pt (II) and Ir (III) complexes, Journal of Chemical Theory and Computation. 11 (2015) 3281–3289.

[72] D. Jacquemin, E. A. Perpète, G. E. Scuseria, I. Ciofini, C. Adamo, TD-DFT Performance for the Visible Absorption Spectra of Organic Dyes: Conventional versus Long-Range Hybrids, Journal of Chemical Theory and Computation. 4 (2007) 123–135.

[73] D. Jacquemin, E. A. Perpète, G. Scalmani, M. J. Frisch, R. Kobayashi, C. Adamo, Assessment of the efficiency of long-range corrected functionals for some properties of large compounds, The Journal of Chemical Physics. 126 (2007) 144105.

[74] E. A. Perpète, F. Maurel, D. Jacquemin, TD-DFT investigation of diarylethene dyes with cyclopentene, dihydrothiophene, and dihydropyrrole bridges, Journal of Physical Chemistry A. 111 (2007) 5528–5535.

[75] E. A. Perpète, J. Preat, J. M. André, D. Jacquemin, An ab initio study of the absorption spectra of indirubin, isoindigo, and related derivatives, Journal of Physical Chemistry A. 110 (2006) 5629–5635.

[76] J. L. Liao, P. Rajakannu, S. H. Liu, G. H. Lee, P. T. Chou, A. K. Y. Jen, Y. Chi, Iridium(III) Complexes Bearing Tridentate Chromophoric Chelate: Phosphorescence Fine-Tuned by Phosphine and Hydride Ancillary, Inorganic Chemistry. 57 (2018) 8287–8298.

[77] M. Seth, T. Ziegler, Range-separated exchange functionals with Slater-type functions, Journal of Chemical Theory and Computation. 8 (2012) 901–907.

[78] A. A. Al-Amiery, A. A. H. Kadhum, A. B. Mohamad, Antifungal and antioxidant activities of pyrrolidone thiosemicarbazone complexes, Bioinorganic Chemistry and Applications. (2012) 1–6.

[79] S. Shaygan, H. Pasdar, N. Foroughifar, M. Davallo, F. Motiee, Cobalt (II) Complexes with Schiff Base Ligands Derived from Terephthalaldehyde and ortho-Substituted Anilines: Synthesis, Characterization and Antibacterial Activity, Applied Sciences. 8 (2018) 385.

[80]   B. B. Beyene, A. M. Mihirteu, M. T. Ayana, A. W. Yibeltal, Synthesis, characterization and antibacterial activity of metalloporphyrins: Role of central metal ion, Results in Chemistry. 2 (2020) 100073.

[81]   E. Kouris, S. Kalogiannis, F. Perdih, I. Turel, G. Psomas, Cobalt(II) complexes of sparfloxacin: Characterization, structure, antimicrobial activity and interaction with DNA and albumins, Journal of Inorganic Biochemistry. 163 (2016) 18–27.

[82]   S. Mohanapriya, Muthukumaran, S. Vairam, Synthesis, characterization, thermal behavior and antimicrobial activity of 3-methyl benzoate complexes of transition metal with hydrazine, Bull Chem Soc Ethiop. 30 (2016) 241–252.

[83]   M. Jafari, M. Salehi, M. Kubicki, A. Arab, A. Khaleghian, DFT studies and antioxidant activity of Schiff base metal complexes of 2-aminopyridine. Crystal structures of cobalt(II) and zinc(II) complexes, InorganicaChimica Acta. 462 (2017) 329–335.

[84]   A. Benhassine, H. Boulebd, B. Anak, A. Bouraiou, S. Bouacida, M. Bencharif, A. Belfaitah, Cobalt(II) complexes based on (1-methyl-1H-benzo[d]imidazol-2-yl) methanol derivative: synthesis, crystal structure, spectroscopy, DFT calculations, and antioxidant activity, Journal of Coordination Chemistry. 71 (2018) 311–328.

[85]   F. Collin, Chemical Basis of Reactive Oxygen Species Reactivity and Involvement in Neurodegenerative Diseases, International Journal of Molecular Sciences. 20 (2019) 2407.

[86]   C. Wang, Y. Wu, Y. Qu, K. Zhao, J. Xu, X. Xia, H. Wu, Synthesis, structure and antioxidant properties of manganese(II), zinc(II) and cobalt(II) complexes with bis(benzimidazol-2-ylmethyl)allylamine, Transition Metal Chemistry. 45 (2020) 523–529.

[87] G. Swiderski, A. Jabłonska-Trypuc, M. Kalinowska, R. Swisłocka, D. Karpowicz, M. Magnuszewska, W. Lewandowski, Spectroscopic, Theoretical and Antioxidant Study of 3d-Transition Metals (Co(II), Ni(II), Cu(II), Zn(II)) Complexes with Cichoric Acid, Materials. 13 (2020) 3102.

[88] U. Sani, S. Dailami, Synthesis, Characterization, Antimicrobial Activity and Antioxidant Studies of Metal (II) Complexes of Schiff Base Derived from 2 – Hydroxy - 1- Naphthaldehyde and Hydrazine Monohydrate, ChemSearch Journal. 6 (2016) 35–41.

[89] S Trifunschi, D Ardelean, Synthesis, characterization and antioxidant activity of Co (II) and Cd (II) complexes with quercetin, Revista De Chimie . 67 (2016) 2422–2424.

[90] N. Amiri, S. Nouir, M. Hajji, T. Roisnel, T. Guerfel, G. Simonneaux, H. Nasri, Synthesis, structure, photophysical properties and biological activity of a cobalt(II) coordination complex with 4,4'-bipyridine and porphyrin chelating ligands, Journal of Saudi Chemical Society. 23 (2019) 781–794.

[91] W. Lad, A. O'connar, L. Latore, O. Dennis, S. Ringer, J. A. Whittaker, J. Conrad, B. Vogler, H. Rosner, W. Kraus, the in vitro anti-denaturation effects induced by natural products and non-steroidal compounds in heat treated (immunogenic) bovine serum albumin is proposed as a screening assay for the detection of anti-inflammatory compounds, without the use of animals, in the early stages of the drug discovery process, West Indian Medical Journal. 57 (2008) 327–331.